

¹ Topographic Effects on Internal Waves at
² Barkley Canyon

³ Kurtis Anstey
⁴ V00939802
⁵ Department of Physics and Astronomy
⁶ University of Victoria
⁷ February 21, 2022

⁸ Dr. Jody Klymak (University of Victoria)
⁹ Dr. Steven Mihaly (Ocean Networks Canada)
¹⁰ Dr. Richard Thomson (Institute of Ocean Sciences)

11 Table of Contents

12	List of Figures	3
13	1 Abstract	4
14	2 Introduction	5
15	3 Internal wave theory	8
16	4 Barkley Canyon	12
17	5 Results	18
18	5.1 Observations	18
19	5.1.1 Mean currents	18
20	5.1.2 High frequency currents	18
21	5.1.3 Depth dependence	22
22	5.2 Frequency-dependent response	24
23	5.2.1 Sub-diurnal	24
24	5.2.2 Diurnal	26
25	5.2.3 Near-inertial	29
26	5.2.4 Semidiurnal	33
27	5.2.5 Continuum	36
28	5.2.6 Shoulder	42
29	6 Discussion	45
30	6.1 Canyon axis mean currents	45
31	6.2 Tidal forcing	46
32	6.3 Near-inertial forcing	49
33	6.4 Continuum-dissipation estimates	51
34	6.5 Spectral shoulder energy	52
35	7 Summary and conclusions	53
36	8 Appendix A: Supplemental plots	56
37	8.1 Wind comparisons	56
38	9 References	59

39 List of Figures

40 1	IW processes	6
41 2	IW in a two-layer system	7
42 3	IW and topography	8
43 4	Barkley Canyon site map and semidiurnal criticality	9
44 5	Site topography	10
45 6	ADCP frequency, instrument ID, deployment, and data availability	13
46 7	QA threshold profiles	14
47 8	Mean stratification and WKB scaling factor	15
48 9	Low-pass velocities	17
49 10	Axis along-canyon mean-flow	19
50 11	High-pass velocities - April 2013	20
51 12	PSD and rotary spectra	21
52 13	Depth-frequency PSD	23
53 14	Depth-band PSD - Sub-diurnal	25
54 15	Depth-band PSD - Diurnal	27
55 16	Diurnal spring-neap forcing	28
56 17	Depth-band rotary PSD - Near-inertial	30
57 18	NI vertical energy propagation	31
58 19	NI delayed deep response histogram	31
59 20	NI slab response - 2013	32
60 21	NI vertical modes	33
61 22	Depth-band PSD - Semidiurnal	34
62 23	Semidiurnal spring-neap forcing	35
63 24	Depth-band PSD - Continuum	37
64 25	Continuum power law fits	38
65 26	Dissipation and diffusivity	39
66 27	Dissipation power law fits	40
67 28	Dissipation multi-variate power law fits	42
68 29	Depth-band PSD - Shoulder	43
69 30	Shoulder-dissipation power law fits	44
70 31	High frequency-resolution PSD - 2013	50
71 32	Appendix A - NI wind comparisons - 2014	56
72 33	Appendix A - NI wind comparisons - 2017	57
73 34	Appendix A - NI wind comparisons - 2018	58

74 1 Abstract

75 At two Barkley Canyon sites (the continental slope below the shelf-break, and
76 deep within the canyon), four overlapping years of horizontal velocity time-
77 series data are used to examine the effects of irregular topography on the inter-
78 internal wave field. Mean currents are topographically guided at both sites, and in
79 the canyon there is an inter-annually consistent, periodic (about a week) up-
80 canyon flow (-700 to -900 m) above a near-bottom down-canyon layer. There
81 is elevation of internal wave energy near topography, up to a factor of 10, 130
82 m above the slope, and up to a factor of 100, 230 m above the canyon bottom.
83 All bands display inter-annually consistent, frequency-dependent seasonality.
84 Sub-diurnal and diurnal flows are sub-inertially trapped along topography, and
85 the diurnal band appears to be forced locally (barotropically). Both sites have
86 high NI energy. At the slope site, NI energy is attenuated with depth, while in
87 the canyon NI energy is amplified near the bottom. Both sites show intermit-
88 tent NI forcing associated with wind events, high-mode propagation, and the
89 seasonal mixed-layer depth, though fewer events are observed in the canyon.
90 Free semidiurnal internal tides are focused and reflected near critical shelf-
91 break and canyon floor topography, and appear to experience both local and
92 remote (baroclinic) forcing. The high-frequency internal wave continuum has
93 enhanced amplitudes near bottom at both sites (up to 7× open-ocean GM),
94 and inferred dissipation rates, ϵ , increasing from a background of less than
95 10^{-9} W/kg to exceeding 10^{-8} W/kg. Dissipation is most strongly correlated
96 with the semidiurnal (M_2) constituent at both sites, with secondary contribu-
97 tions from the sub-diurnal (Sub_K1) band on the slope, and the NI band in
98 the canyon. Power laws for these dependencies are $\epsilon \sim M_2^{0.83} + \text{Sub}_{K1}^{0.59}$ at the
99 slope, and $\epsilon \sim M_2^{1.47} + \text{NI}^{0.24}$ in the canyon. There is evidence of a near- N
100 spectral shoulder correlated with continuum energy, with a power law fit of
101 $P_{Sh} \sim \epsilon^{0.34 \pm 0.08}$ that is independent of site topography. Though some general
102 results are expected from observations at other slope and canyon sites, it seems
103 that regional characteristics may make for unique, site-dependent forcing of
104 internal wave driven processes.

105 2 Introduction

106 Internal waves (IW) are slow-moving, low-frequency, sub-surface gravity waves
107 that exist within density gradients in the ocean interior (Garrett & Munk,
108 1979). They have horizontal wavelengths up to kilometres long, and oscillate
109 in a range between the local Coriolis (inertial, f) and Brunt–Väisälä (buoy-
110 ancy, N) frequencies (Garrett & Munk, 1979). They are forced by weather -
111 as near-inertial (NI) IW generated by surface winds exciting currents in the
112 mixed layer (ML) that pump energy into the interior (Garratt, 1977) - or
113 by tides and currents moving across irregular seafloor topography, generating
114 baroclinic internal tides (IT) and IW that can propagate through the stratified
115 ocean (Hendershott & Garrett, 2018). As travelling IW approach irregular to-
116 pography, such as continental slopes or submarine canyons, they can focus and
117 break, leading to elevated mixing. As mixing can be linked to ocean circula-
118 tion, biogeochemical cycles, weather, and long-term climate (Kunze, 2017), it
119 is important to understand forcing by the IW field. As incident IW and IT
120 have varying origins, amplitudes, and frequencies, each responds differently
121 to the influence of impacted topography. Sub-inertial IW and IT may be
122 trapped along topography, while those that are NI or super-inertial are free
123 to reflect and propagate through open water. By characterising the IW and
124 IT that comprise the local IW field, it may be possible to better quantify and
125 understand IW driven turbulence and mixing.

126 The wind, currents, and tides are ever-present, and IW are prevalent ocean
127 phenomena. As early as the mid-19th century, notable scientists such as Stokes
128 and Rayleigh were investigating properties of fluid density and stratification,
129 essential for IW propagation (Garrett & Munk, 1979). IW were mistaken
130 as consistent noise in early 20th-century hydrocast readings, and Ekman dis-
131 cussed their effects in his seminal theories on fluid mechanics (Garrett & Munk,
132 1979). In the late-20th century, Garrett and Munk (1979) developed the canon-
133 ical Garrett-Munk (GM) spectrum defining the characteristic frequency and
134 wavenumber continuum of open-ocean IW, to better understand their role in
135 ocean processes. Instrumentation improved, and scientists continued to un-
136 cover the contributions of IW to physical systems of all scales, from fine-scale
137 mixing to the large-scale meridional overturning circulation (Figure 1; Garrett
138 & Munk, 1979). Recently, studies have linked IW generation and dissipation to
139 the global oceanic energy budget (Carter & Gregg, 2002; Kunze et al., 2002;
140 Terker et al., 2014; Kunze, 2017), tide and wind forcing of IW to seasonal
141 variability of regional circulation processes (Alford et al., 2012; Thomson &
142 Krassovski, 2015), and enhanced mixing to IW interactions with irregular to-
143 pography (Nash et al., 2004; Kunze et al., 2012; Gemmrich & Klymak, 2015).

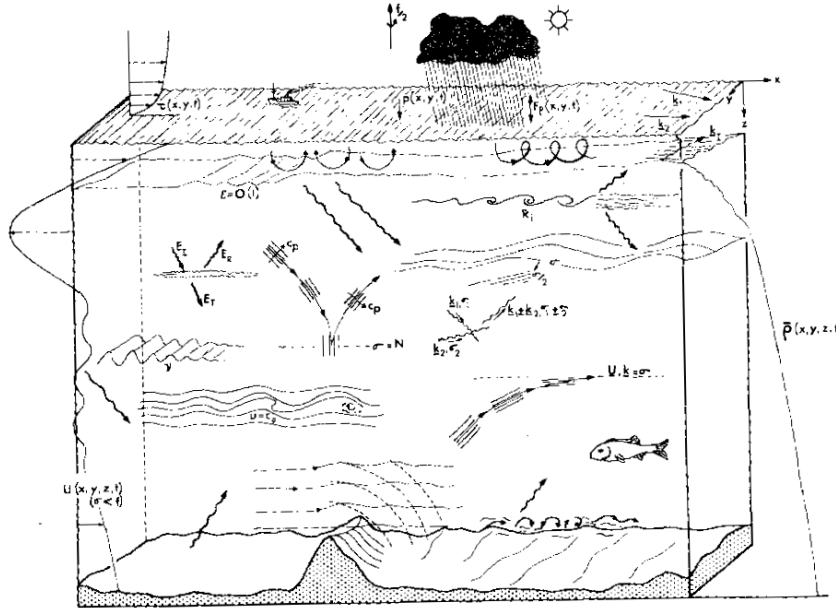


Figure 1. Generalised depiction of IW processes in the ocean, as envisioned by Garrett and Munk (1979). IW are forced by, coincide with, or contribute to most physical processes in the ocean.

- 144 Further research on IW interactions with irregular topography is thought to
 145 be essential to understanding seasonal upwelling, diapycnal mixing, and cross-
 146 shelf exchange (Burrier, 2019). As IW and IT approach seamounts, slopes,
 147 or canyons, nonlinear processes may cause their energy to reflect, scatter,
 148 or focus and break (Figure 3), dissipating as heat (Garrett & Munk, 1979;
 149 Klymak et al., 2006; Kunze et al., 2012). Dissipation leads to an energetic
 150 local environment, evident as near-bottom turbulent processes on the fine- (1
 151 - 100 m vertical) and micro-scales (< 1 m vertical) (Garrett & Munk, 1979;
 152 Carter & Gregg, 2002; Kunze et al., 2002; Kunze et al., 2012). These processes
 153 lead to the elevated mixing of pollutants and biological constituents, and drive
 154 regional transport of energy and momentum (Kunze et al., 2012). Topography-
 155 forced IW mixing helps set ocean stratification, layers that even influence the
 156 large-scale ocean-atmosphere coupled climate system (Garett & Munk, 1979).
- 157 In Canada, IW are regularly observed on the highly productive Vancouver
 158 Island Continental Shelf (VICS) (Thomson & Crawford, 1982; Allen et al.,
 159 2001), a relatively broad (about 80 km) shelf region featuring a canyon-incised
 160 continental slope. Regional observations have led to insight on non-linear
 161 wave-wave interactions between surface generated NI IW and upward propa-
 162 gating semidiurnal IT (Mihaly et al., 1998), and the presence of diurnal baro-
 163 clinic shelf waves forced by tidal oscillations near the mouth of the Juan de

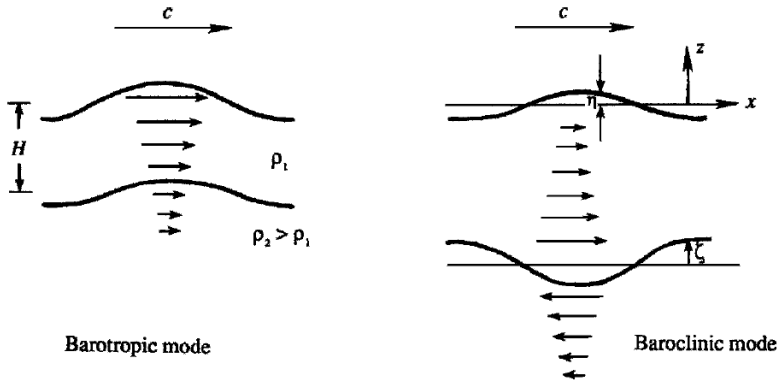


Figure 2. IW in a two-layer system. Graphic representation of the difference between barotropic and baroclinic flows. Adapted from Kundu & Cohen (2008).

164 Fuca Strait (Thomson & Crawford, 1982). Seasonally variable regional currents (Thomson & Krassovski, 2015) have been associated with observations
 165 of vorticity stretching and upwelling at the head of the shelf-incising Barkley
 166 Canyon, suggesting considerable canyon influence on VICS water properties,
 167 transport of biological constituents, and overall shelf productivity (Allen et al.,
 168 2001; Juniper et al., 2013; Doya et al., 2013; Chauvet et al., 2018). However,
 169 there is a lack of topography-IW observations at Barkley Canyon necessary
 170 to properly characterise its influence on the physical processes of the VICS.
 171 Further research into Barkley Canyon's IW field can provide insight into the
 172 effects of topography-driven mixing on the productivity of not only the VICS,
 173 but global shelf sites adjacent to canyon-incised continental slopes.
 174

175 This study evaluates horizontal velocity data from two Barkley Canyon sites,
 176 one on the adjacent continental slope and one within the canyon, to charac-
 177 terise the topography interactions of IW and IT, and their potential influence
 178 on local mixing. Mean currents, and IW of sub-tidal, tidal, NI, and super-tidal
 179 (IW continuum and near- N spectral shoulder) frequency bands are evaluated
 180 for depth-dependence and seasonality, including a forcing analysis of variability
 181 due to regional currents, tides, and wind. The high-frequency IW continuum
 182 is evaluated for topographic influence by comparison with open-ocean GM
 183 theory, leading to approximations of dissipation and diffusivity to estimate
 184 mixing. The seasonal energy of the continuum is correlated to low-frequency
 185 constituents to identify which bands contribute most to high-frequency tur-
 186 bulent processes. Key findings include deep-canyon topography-guided cur-
 187 rent layers, near-topography focusing of IW energy with frequency-dependent
 188 seasonality and forcing, attenuation of downward NI IW energy above the

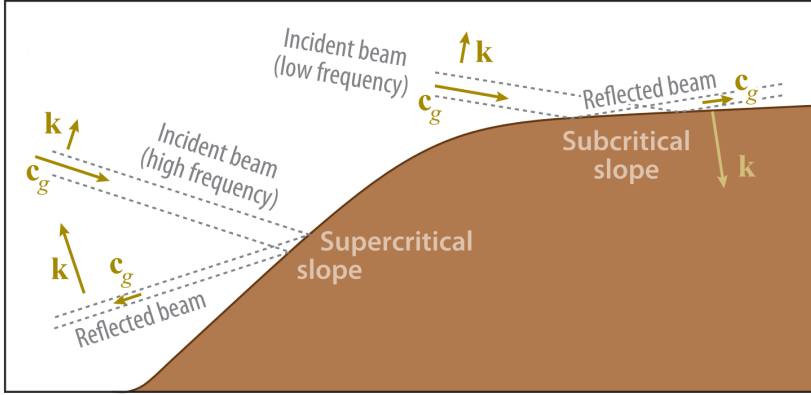


Figure 3. Graphic of IW interactions with slope topography (Lamb, 2014). The propagation angle of an IW depends on frequency and stratification. Depending on the slope of topography, incident IW can be scattered up, reflected down, or focused, possibly breaking.

189 continental slope, elevated high-frequency IW continuum energy linked to the
 190 semidiurnal constituent, and an energetic near- N spectral shoulder that is
 191 seasonally correlated with continuum energy.

192 3 Internal wave theory

193 Vertical displacements in a fluid can be classified as either barotropic, where
 194 the displacement is dependent only on pressure, $P(z)$ (where z is depth),
 195 or as baroclinic, where the displacement is also a function of density, $\rho(z)$,
 196 temperature, $T(z)$, etc. (Figure 2). For example, surface tides are barotropic,
 197 affecting most of the water column as the surface oscillates, while IW are
 198 baroclinic, perturbations that exist along density interfaces in the stratified
 199 ocean interior. IW are highly dependent on stratification, characterised by
 200 the depth-dependent buoyancy frequency, $N(z)$, defined as:

$$201 \quad N^2(z) = -\frac{g}{\rho_0} \frac{d\rho}{dz} \quad (1)$$

202 where g is the acceleration due to gravity, and ρ_0 a constant reference density.
 203 In continuously stratified fluids such as the ocean interior, IW may exist both
 204 non-isotropically and rotationally, with the relative effects of clockwise (CW)
 205 and counter-clockwise (CCW) rotation described by the consistency relation:

$$206 \quad \frac{CW}{CCW} = \frac{(\omega + f)^2}{(\omega - f)^2} \quad (2)$$

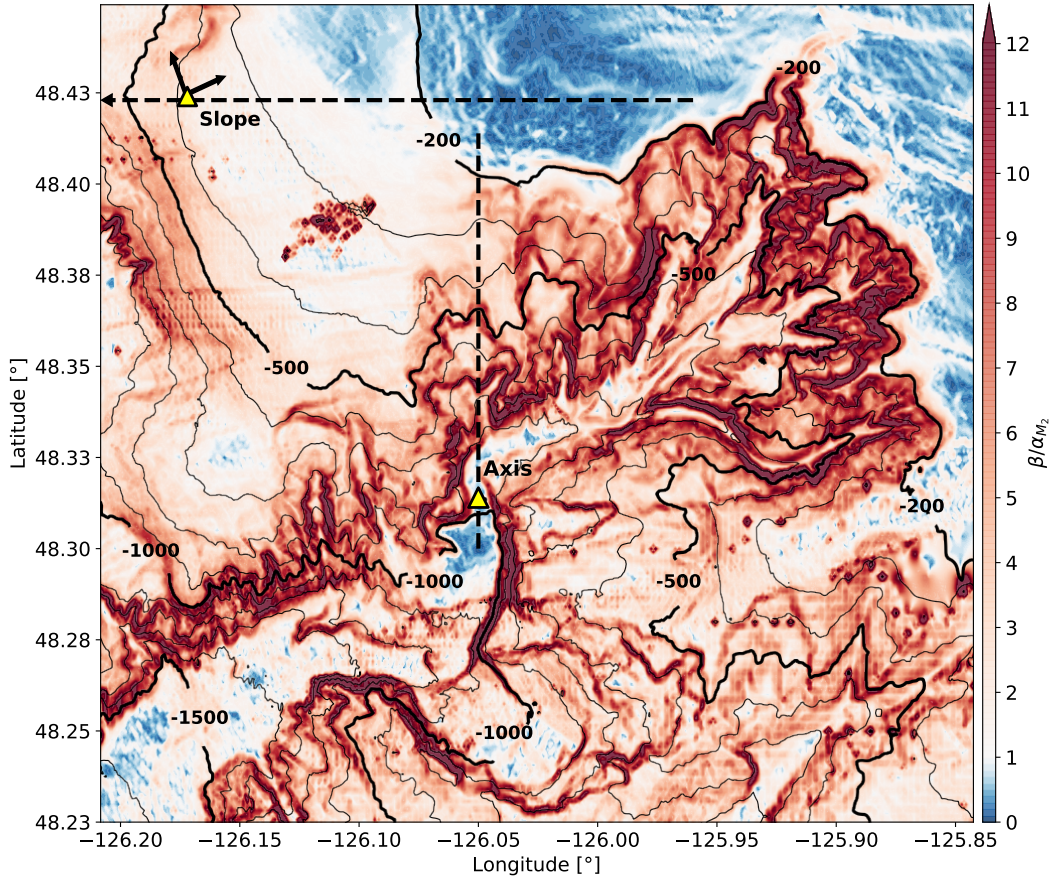


Figure 4. Site map and semidiurnal criticality of Barkley Canyon. Criticality is found by dividing the gradient slope (β) of topography by the depth-dependent semidiurnal propagation angle (α_{M_2}). Most of the region is supercritical (> 1) to the M_2 IT, with notable exceptions on the shelf and canyon floor near the Axis site. Arrows at the Slope site indicate 30° rotation of velocity data to match approximate along-slope (v) direction of mean currents; Axis data were not rotated, as the along-canyon (v) component is aligned N-S. Dashed black lines indicate topography cross-sections used in Figure 5.

where ω is frequency, and f the Coriolis frequency ($f = 2\Omega \sin \phi$, where Ω is the rotation rate of the Earth, and ϕ is latitude). f and $N(z)$ are the lower and upper frequency bounds for free IW (Kundu & Cohen, 2008). IW generated outside this frequency range are evanescent (trapped) to topography, unable to radiate into the ocean interior (Flather, 1988).

As free IW and IT approach irregular topography (continental slopes, canyons, etc.), the angle of the incident wave ray, α , and the slope of the topography, β , have an influential relationship on the behaviour of the topography-IW interaction (Figure 3) (Lamb, 2014). The ray path of an incident, free IW in

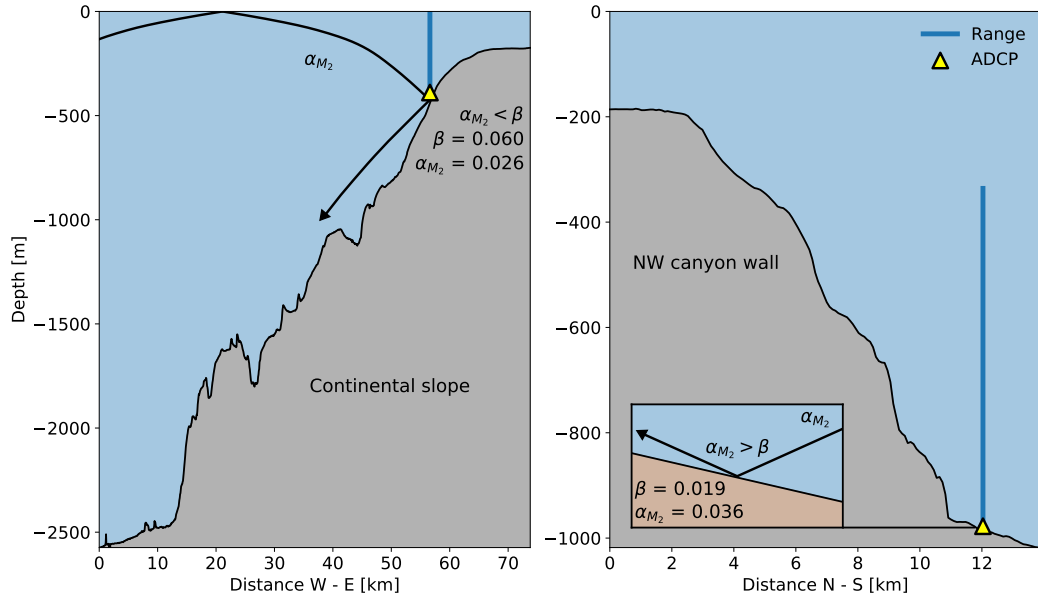


Figure 5. Site topography cross-sections with ray tracing. Depicted are the relative locations for Slope (left) and Axis (right) instrument moorings. Horizontal cross-sections were taken in the W-E (Slope) and N-S (Axis) directions, represented by the dashed black lines in Figure 4. Slope sits below the VICS shelf-break while Axis is located on the floor of Barkley Canyon (right). An incident ray is shown for M_2 , accounting for depth-dependent stratification, as well as local criticality at each site. α is the angle of propagation, and β is the slope of the topography. In general, the Slope region is supercritical, while the Axis region is both subcritical (floor) and supercritical (walls).

216 a continuously stratified fluid is (Nash et al., 2004; Garrett & Kunze, 2007;
 217 Lamb, 2014):

$$218 \quad \alpha(z) = \sqrt{\frac{(\omega^2 - f^2)}{(N(z)^2 - \omega^2)}} \quad (3)$$

219 The impacted bathymetric slope, $\beta = \nabla H$, is determined from the gradient
 220 magnitude of the local topography, and used to determine regions of IW and
 221 IT criticality, as in Figure 4 (Martini et al., 2011). As α depends on $N(z)$,
 222 the characteristic ray path of an IW bends with depth. If $\beta > \alpha$, the slope is
 223 supercritical and incident wave energy is reflected downward (see Figure 5); for
 224 $\beta \approx \alpha$, the slope is near-critical and incident wave energy is focused, potentially
 225 leading to non-linear breaking and dissipation; and, for $\beta < \alpha$, the slope is
 226 considered subcritical and incident wave energy is scattered upward (Klymak
 227 et al., 2011). The combined effects of reflection, scattering, and focusing of IW
 228 and IT in near-critical regions can lead to an energetic layer near topography
 229 (Lamb, 2014). Intensified near-slope layers are not uncommon (Polzin et al.,
 230 1997; Nash et al., 2004; Kunze et al., 2012), and can elevate IW energy multiple

231 orders of magnitude with depth-dependent vertical scales hundreds of metres
 232 above bottom (Hotchkiss & Wunsch, 1982; Gemmrich & Klymak, 2015), in
 233 turn elevating mixing.

234 The energetic mixing regions near-critical to tidal frequencies are also known
 235 as hot-spots for generation of baroclinic IT, including continental slope, shelf-
 236 break, and canyon topography, though IT can also be generated over non-
 237 critical irregular topography through frictional tidal oscillations (Garrett &
 238 Kunze, 2007). Topographically generated free IT can radiate away baroclin-
 239 ically, potentially impacting distant topography, dissipating their energy re-
 240 motely (Kunze et al., 2012). At latitudes where an oscillating tidal frequency
 241 is sub-inertial and generated IT are trapped to topography, baroclinic 'shelf
 242 waves' may be generated over irregular topography and propagate along the
 243 continental margin where the topographic gradient of the shelf acts as a restor-
 244 ing force for horizontal propagation (Crawford & Thomson, 1984; Brink, 1991).

245 In addition to topographically generated IW and IT, there is significant input
 246 into the oceanic IW field from wind (Alford et al., 2016). NI energy is deposited
 247 into the surface mixed-layer (ML), forcing NI currents that 'strum' IW modes;
 248 the relative rotation and propagation of these modes moves energy downward
 249 to the base of the thermocline, then into the interior (Zervakis & Levine, 1995).
 250 Generated NI IW propagate downward and equatorward into the ocean interior
 251 (Alford et al., 2016). For a flat-bottom basin bounded by the ocean surface,
 252 the vertical structure of IW modes exist as solutions to the Sturm-Liouville
 253 equation:

$$\frac{\partial^2}{\partial z^2}\eta(z) + \frac{N^2(z)}{c_n^2}\eta(z) = 0 \quad (4)$$

254 with boundary conditions $\eta(0) = \eta(D) = 0$, where D is the total water depth,
 255 η is surface displacement, n the mode number, and c_n the modal eigenspeed
 256 (Alford & Zhao, 2007). Low-modes tend to dominate NI IW energy and largely
 257 propagate laterally, while high-mode energy typically radiates downward (Al-
 258 ford et al., 2016). Seasonal NI mode amplitudes can be found using ML depth
 259 as a time-dependent step-function convolved with ML NI currents, as deter-
 260 mined by a 'slab' model (discussed in Section 4). In general, the superposition
 261 of many modes forms an IW beam (Lamb, 2014). The downward propagation
 262 of IW energy is then defined by the dispersion relation:

$$c_{gz} = \frac{\omega^2 - f^2}{\omega m} \quad (5)$$

263 where m is the vertical wavenumber (Alford et al., 2012; Alford et al., 2013).

266 As IW and IT generated by sub-tidal, tidal, and NI processes propagate and
267 impact irregular topography, they may break. Incident low-frequency IW en-
268 ergy cascades to the high-frequency IW continuum, and can result in the
269 formation of strong along-slope currents and density overturns, ultimately re-
270 sulting in mixing (Lamb, 2014). Breaking can occur due to a variety of pro-
271 cesses; for example, shoaling IW can overturn, and barotropic tidal currents
272 can generate breaking lee waves and hydraulic jumps over irregular topography
273 (Lamb, 2014). Linear inviscid theory predicts that when downward propagat-
274 ing IW and IT impact a near-critical slope, the reflected wave amplitudes
275 become infinite as group velocity and wave length approach zero, leading to
276 instability (Lamb, 2014). Even when impacting non-critical slopes, incident
277 IT can cause isopycnals to steepen and form unstable 'internal bores' which
278 break and drive turbulent fluid up-slope (Martini et al., 2013). Whatever
279 the mechanism, near-topography IW interactions energise the IW continuum,
280 observations of which can be used to estimate elevated dissipation rates and
281 mixing.

282 4 Barkley Canyon

283 The obtained Barkley Canyon horizontal velocity data are unique for both spa-
284 tial and temporal consideration. Located at approximately 48.33°N 126.03°W,
285 the Barkley Canyon region is about 75 km southwest of the coast of Vancouver
286 Island, incising the continental slope and shelf (Figure 4). Barkley Canyon is a
287 winding canyon up to 6 km wide and 13 km long, with an adjacent shelf-break
288 region beginning around -150 m depth. Spread across the region, Acoustic
289 Doppler Current Profilers (ADCP) provide current data for Ocean Networks
290 Canada's (ONC) NEPTUNE cabled observatory. ADCP emit acoustic beams
291 that triangulate Doppler shifts in the water column, providing directional ve-
292 locity data time series through depth. The placement of ADCP across both
293 continental slope and canyon topography allows for spatial analysis of coin-
294 ciding IW events. Furthermore, ONC's Oceans 2.0 data portal offers publicly
295 available processed data for each instrument, spanning over a decade. As such,
296 the obtained datasets are substantially lengthy for IW research, allowing for
297 typically difficult analysis of long-term variability.

298 The two ADCP for this study are located at the upper continental slope Upper
299 Slope (Slope) and canyon-floor Axis sites (Figure 4). The Slope platform sits
300 below the VICS shelf-break at a depth of -378 m (Figure 5), 15 km NW of
301 Barkley Canyon, employing primarily 75 kHz ADCPs. The Axis platform is
302 located at a narrow north-south channel on the floor of Barkley Canyon, about
303 midway along its length at a sharp bend, and a depth of -968 m (Figure 5),

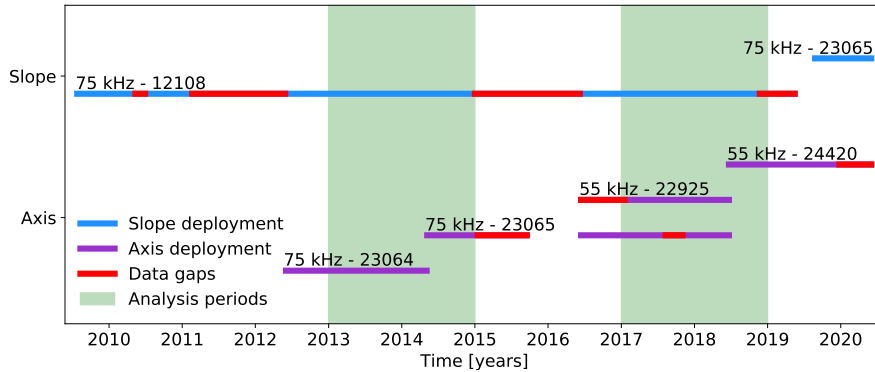


Figure 6. ADCP operating frequency, instrument ID, deployment periods, and data availability for the Slope and Axis sites. ONC operates and maintains regional instruments as part of the NEPTUNE cabled observatory. Due to maintenance and redeployment, years with comprehensive overlapping coverage (2013, 2014, 2017, and 2018) were selected for analysis.

304 employing both 75 and 55 kHz ADCPs. The 75 kHz Teledyne RDI Workhorse
 305 Long Ranger instruments were set to a vertical resolution of 8 m depth bins,
 306 and a continuous sampling rate of 2 seconds. The 55 kHz Nortek Signature55
 307 instrument was set to a vertical resolution of 20 m depth bins, and a pulsed
 308 sampling rate of six 18-second pings followed by a 4.5-minute delay. For these
 309 sites, overlapping data coverage of good quality (e.g. minimal data gaps) is
 310 during 2013, 2014, 2017, and 2018 (Figure 6), due to ONC deployment and
 311 maintenance schedules.

312 An initial quality check of backscatter intensity and beam correlation was
 313 performed for the raw data (Figure 7), yielding quality thresholds of 65 and 115
 314 counts, respectively. There is some seasonal variation in the vertical percent-
 315 good profiles based on these thresholds, notably in the fall, likely associated
 316 with seasonality of biological scatterers higher in the water column. Time-
 317 averaged profiles indicate regions of good data ($\geq 90\%$ good) below -50 m
 318 at Slope, and below -700 m at Axis. These depths avoids near-surface side-
 319 lobe contamination, and depth-dependent processing artifacts - non-physical
 320 high-frequency spikes in power spectra evident above about -600 m. For Axis
 321 instruments, with range well above the cut-off depth, up to -600 m is retained
 322 in plots for reference, and a line at -700 m indicates the upper extent of the
 323 analysis region.

324 Datasets were then acquired in 15-minute averaged sampling intervals for each
 325 analysis year, and combined and mapped to standard depth bins. Data gaps
 326 less than 25 hours were interpolated using a linear process. For large data

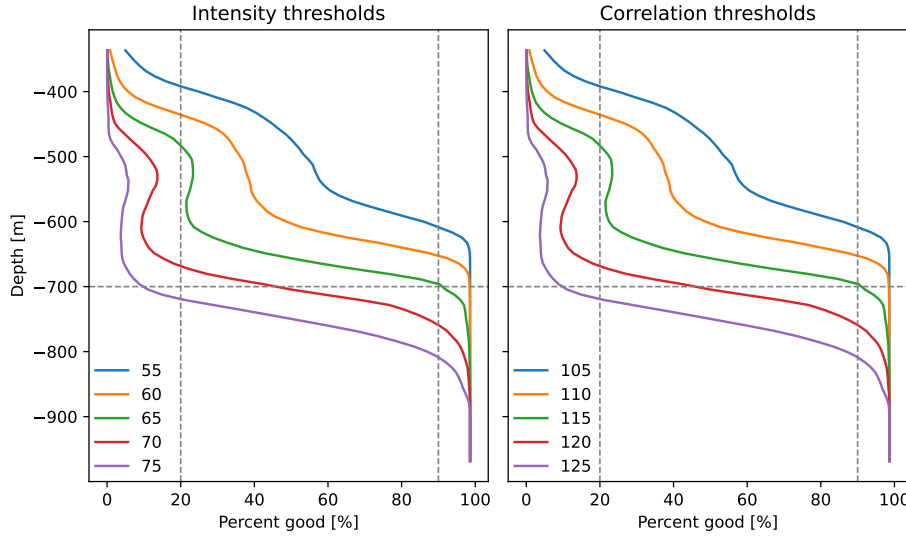


Figure 7. QA threshold profiles. Backscatter intensity and beam correlation percent-good vertical profiles for various thresholds. The green line in each was selected as the ideal threshold value due to the step-function-like steepness of the profile at 20 and 90%, in addition to the qualitative removal of depth-dependent processing artifacts and near-surface side-lobe contamination when used together as a screen.

327 gaps, annual datasets were combined using weighted averaging as necessary.
 328 All supplemental processing materials, including Python code and plots, are
 329 available in a project GitHub repository (Anstey, 2022).

330 At Slope, horizontal velocity data were rotated using a standard rotation ma-
 331 trix:

$$332 \quad u_{rot} = u\cos(\theta) - v\sin(\theta) \quad (6)$$

$$333 \quad v_{rot} = u\sin(\theta) + v\cos(\theta) \quad (7)$$

335 where θ is the rotation angle in radians. This better matches the physical cross-
 336 slope angle of approximately 30° ; u is referred to as cross-slope, and v as along-
 337 slope (Figure 4). At Axis, the along-canyon (v) direction is approximately
 338 north-south, so no rotation was necessary; u is 'cross-canyon'.

339 To account for depth-dependent stratification, horizontal velocity data were
 340 WKB-scaled as:

$$341 \quad u_{WKB}(z) = u(z) \sqrt{\frac{N_0}{N(z)}} \quad (8)$$

342 and for energy density as:

$$343 \quad \phi_{WKB}(z) = \phi(z) \frac{N_0}{N(z)} \quad (9)$$

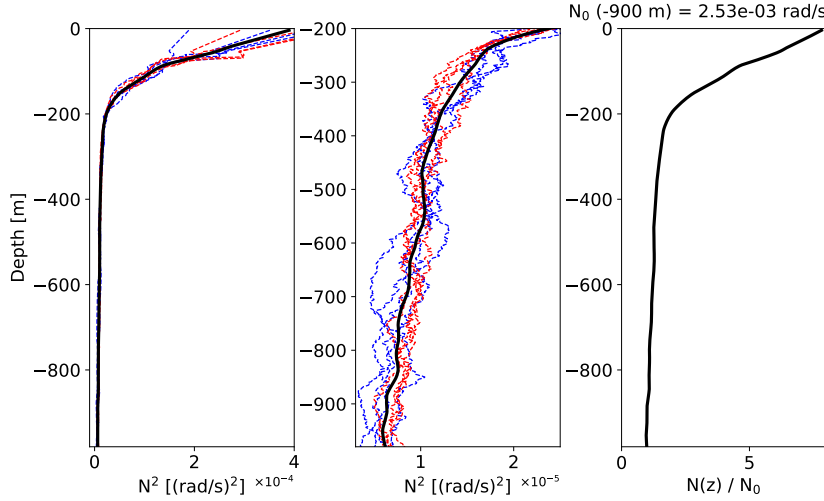


Figure 8. N^2 parameter and WKB scaling factor. Buoyancy results were smoothed and averaged for the four analysis years at La Perouse station LB14 CTD data, and are displayed through the water column (left) and below -200 m (centre). Casts were taken in May (blue) and September (red). A WKB scaling factor (right) was determined for use in Equation 9, based on N_0 averaged around -900 m.

344 with a reference buoyancy frequency of $N_0 = 2.53 \times 10^{-3} \text{ rad/s}$ averaged
 345 around -900 m (Althaus et al., 2003). Buoyancy data were determined from
 346 climatology data obtained from the nearby (20 km S) station LB14. Data were
 347 sampled annually in May and September, during Fisheries and Oceans Canada
 348 (DFO) La Perouse cruises, casting down to -1180 m. Depth profiles were
 349 obtained for temperature, pressure, and salinity, $S(z)$, to find potential density,
 350 $\rho_\theta(z)$, following the UNESCO EOS 80 polynomial (Mamayev et al., 1991).
 351 Depth-dependent buoyancy was then determined as in Equation 1 (Figure 8).
 352 There is little inter-annual variability in the buoyancy depth profiles.
 353 Component-wise power spectral density (PSD) was determined from the WKB-
 354 scaled horizontal velocity data for each depth bin, using a Welch spectrogram
 355 process with a Hanning window of 256 data-points (~ 2.7 days), 50% overlap,
 356 and detrended in time to avoid a 0 Hz offset. Short 1.3 day and long 5.3 day
 357 spectra were also computed. The noise floor of each instrument was deter-
 358 mined from the standard error of the mean relative to instrument sampling
 359 intervals and uncertainties from Nortek and RDI. 95% confidence intervals
 360 were determined using a chi-squared method.
 361 For rotational dependence, rotary power spectra were determined as for PSD,
 362 though using a modified spectrogram process based on the work of Gonella
 363 (1972) and Thomson and Emery (2014). To summarise, the adjustment to find

364 the counter-clockwise (CCW) and clockwise (CW) components of a complex
 365 horizontal velocity vector, $\mathbf{w}(t) = u(t) + iv(t)$, is the addition or subtraction
 366 of twice its quadrature spectrum, Q_{uv} , as:

$$367 \quad \text{CCW} = \frac{1}{2}[S_{uu} + S_{vv} + 2Q_{uv}] \quad (10)$$

$$368 \quad \text{CW} = \frac{1}{2}[S_{uu} + S_{vv} - 2Q_{uv}] \quad (11)$$

370 where S_{uu} and S_{vv} are the typical complex autospectra used for PSD (Thomson
 371 & Emery, 2014). In general, a stronger CW component indicates downward
 372 propagation of energy, and vice-versa.

373 The open-ocean GM IW spectrum was determined using local parameters for
 374 $f = 1.73 \times 10^{-5}$ Hz, $g = 9.81(m/s)^2$, and N_0 , along with canonical values
 375 for the surface-extrapolated buoyancy frequency ($N_{GM} = 5.24 \times 10^{-3}$ rad/s),
 376 e-folding scale of $N(z)$ (1.3×10^3 m), mode scale number $j* = 3$, and dimensionless
 377 IW energy parameter $E = 6.3 \times 10^{-5}$, as in Munk and Wunsch (1998).
 378 The directional GM spectrum was adapted to rotary form through application
 379 of the rotary consistency relation, as described in Section 3 (Levine, 2002;
 380 Polzin & Lvov, 2011).

381 For wind forcing of NI IW, a slab model was conducted as in D'Asaro (1995)
 382 and Alford (2001), providing a simplified idea of the ML response to NI wind
 383 forcing (Alford et al., 2016). Though simple, the model is continuously being
 384 improved to better account for non-homogeneous internal ML processes, and
 385 ML to pycnocline energy transfer (Alford & Zhao, 2007; Jarosz et al., 2007;
 386 Alford et al., 2016; Zheng et al., 2017; Voelker et al., 2020; Alford, 2020).
 387 From surface wind time series, wind stress is calculated as in Garratt (1977):

$$388 \quad \tau_0 = \rho C_D V(z)^2 \quad (12)$$

389 where ρ is the density of air (approximated as 1), $V(z)$ is the complex wind
 390 velocity vector, and C_D is the characteristic drag coefficient determined by:

$$391 \quad C_D \times 10^3 = 0.51V^{0.46} \quad (13)$$

392 For appropriate seasonally, a ML of seasonally varying depth, H , must be
 393 considered. Assuming a null initialisation parameter u_{I1} at time t_1 , wind
 394 generated slab layer currents at time t_2 are then computed as:

$$395 \quad u_{I2} = u_{I1}e^{-\omega\Delta t} - \frac{T_t}{H\omega^2}(1 - e^{-\omega\Delta t}) \quad (14)$$

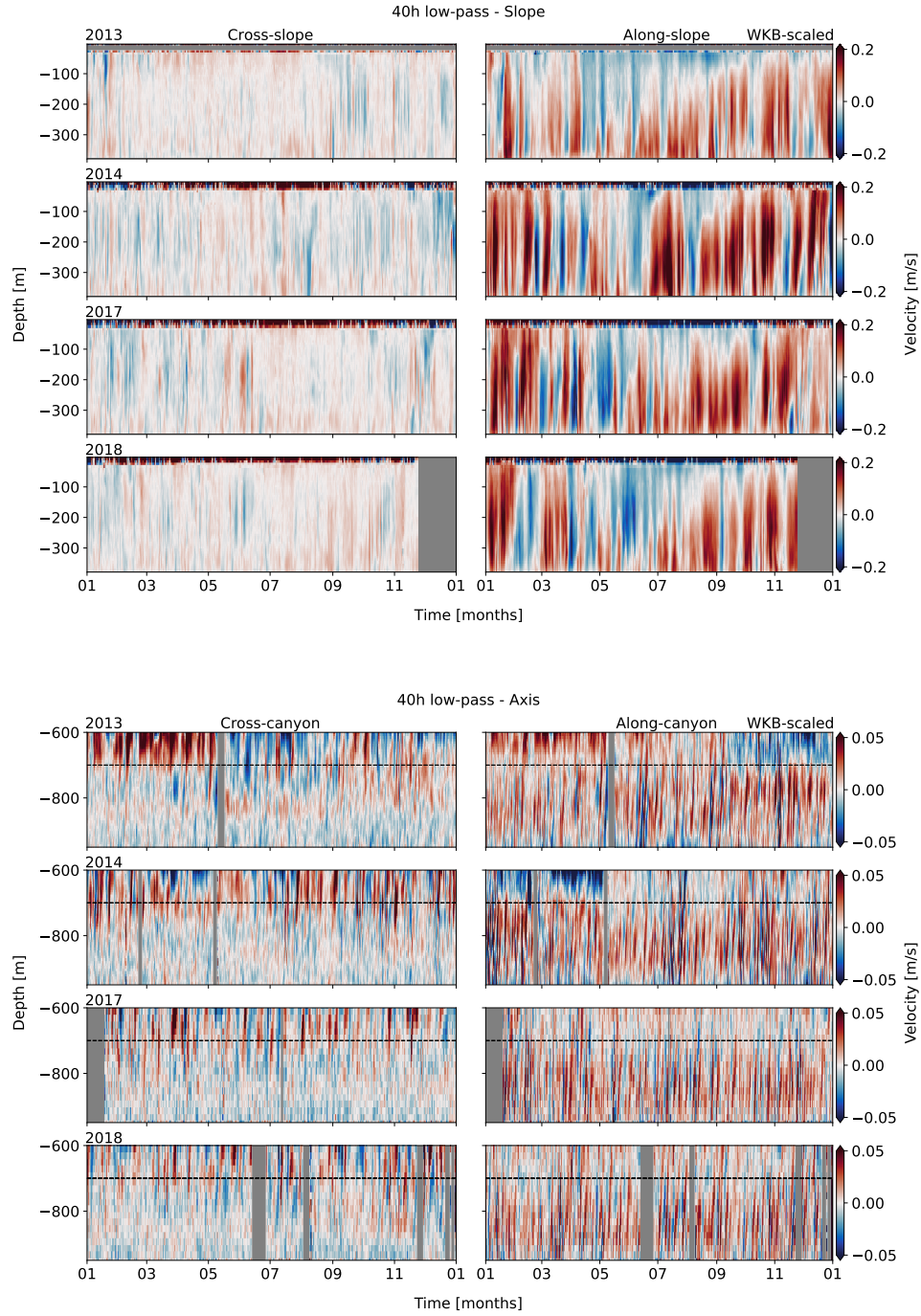


Figure 9. 40-hour low-pass WKB-scaled horizontal velocity data for Slope (top) and Axis (bottom). Components are separated as cross- (left) and along-slope/canyon (right). At Axis, the dashed line is the upper limit of the analysis depths (-650 m). There is a clear seasonal cycle in the along-slope component at Slope, while seasonality is less apparent in the predominantly along-canyon flow at Axis.

396 where a damped rotation frequency, ω , is determined as:

$$397 \quad \omega = r + if \quad (15)$$

398 with $r = 0.15f$ as an artificial damping parameter, as defined in Alford (2001);
 399 and

$$400 \quad T_t = \frac{\Delta T}{\Delta t} \quad (16)$$

401 is related to the complex stress vector, defined as:

$$402 \quad T = \frac{\tau_x + i\tau_y}{\rho_{ML}} \quad (17)$$

403 where $\rho_{ML} = 1024 \text{ kg/m}^3$ is the average density of the ML. The slab currents
 404 are then band-passed for their NI component, u_{NI} .

405 5 Results

406 5.1 Observations

407 5.1.1 Mean currents

408 Regional low-frequency mean currents are inter-annually consistent, topo-
 409 graphically guided, and seasonally site-dependent (Figure 9). To identify long-
 410 term mean currents, a 40-hour, 8th-order, digital low-pass Butterworth filter
 411 was applied to the WKB-scaled horizontal velocity data. There is little inter-
 412 annual variability in mean currents, though each site has unique seasonality.
 413 At Slope, mean currents below -50 m are as expected for this portion of the
 414 California current system (Figure 9): generally poleward along-slope (up to
 415 $> 0.2 \text{ m/s}$) through depth, with a quick transition to upwelling-favourable
 416 equatorward flow in the late-spring (April/May), with the deep poleward cur-
 417 rents shoaling by fall (Thomson & Krassovski, 2015). In the canyon, mean
 418 currents below -700 m are consistently up-canyon (up to $> 0.05 \text{ m/s}$), with
 419 down-canyon flow $< 50 \text{ m AB}$ (Figure 10). A two-week rolling depth-average
 420 between -700 and -900 m yields consistently positive (up-canyon) velocities up
 421 to 0.02 m/s , with annual means of $0.007 - 0.010 \text{ m/s}$. Two-month snapshots
 422 show the up-canyon flow is comprised of shoaling pulses with periodicity of
 423 about a week (Figure 9b). Shoaling is consistent seasonally and inter-annually
 424 (not shown).

425 5.1.2 High frequency currents

426 High-frequency ($< 40\text{-hour}$) velocity data show variable periodicity and verti-
 427 cal structure. Subtracting the 40-hour low-pass currents from the total yields
 428 residual high-frequency currents - flows with periodicity less than 40-hours

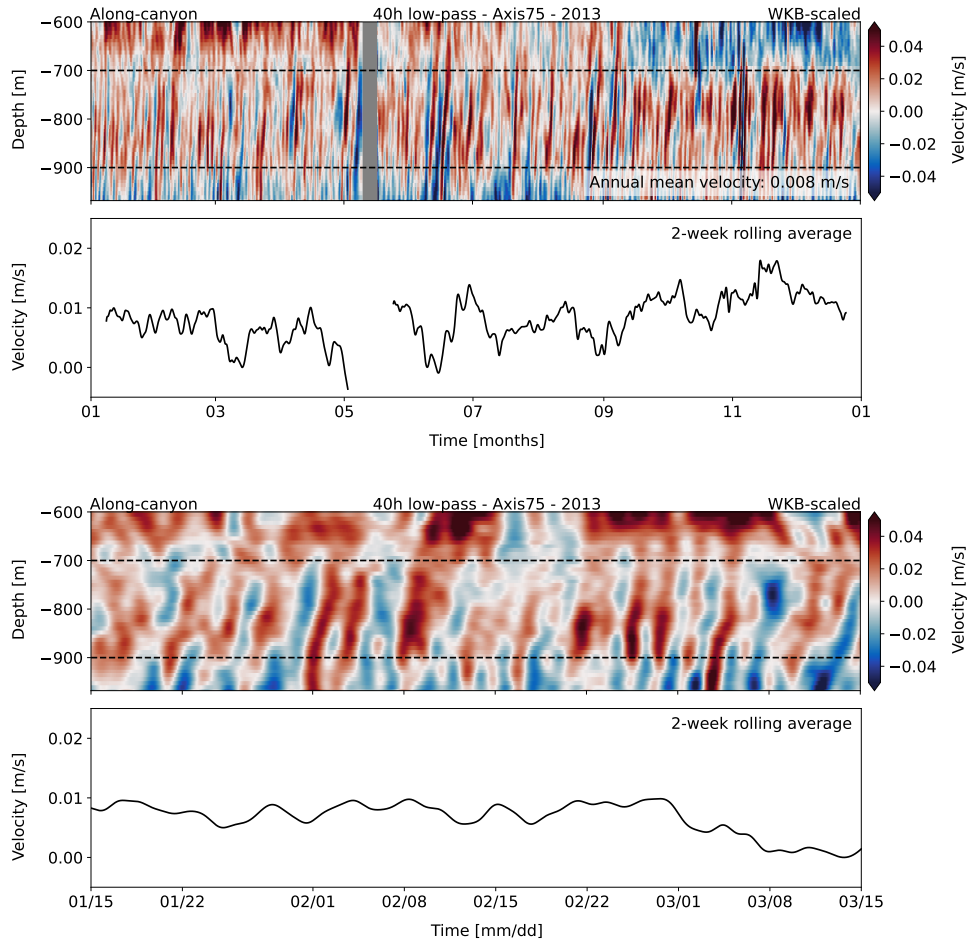


Figure 10. 40-hour low-pass WKB-scaled horizontal velocity data showing along-canyon mean currents for Axis, annually (top) and in a two-month snapshot (bottom). Mean up-canyon flow is within the dashed lines; a thin near-bottom layer of mean down-canyon flow is below.

429 (Figure 11). A two-week snapshot during the annually recurring April/May
 430 mean current transition reveals the presence of tidal and NI IW with non-
 431 uniform vertical structure. At the Slope site, high frequency currents reach
 432 over 0.1 m/s in both cross- and along-slope directions, and there is periodic
 433 shoaling above -250 m depth (about 150 m AB). At Axis, high-pass currents
 434 are strongest below -750 m (about 250 m AB), up to about 0.2 m/s and mostly
 435 along-canyon, with increased non-uniformity in the vertical structure above.
 436 Annual mid-depth (-195 m and -800 m) power spectra of the high frequency
 437 currents at each site show strong tidal and NI influence (Figure 12), with
 438 site- and frequency-dependent topographic guiding. Inter-annual variability is

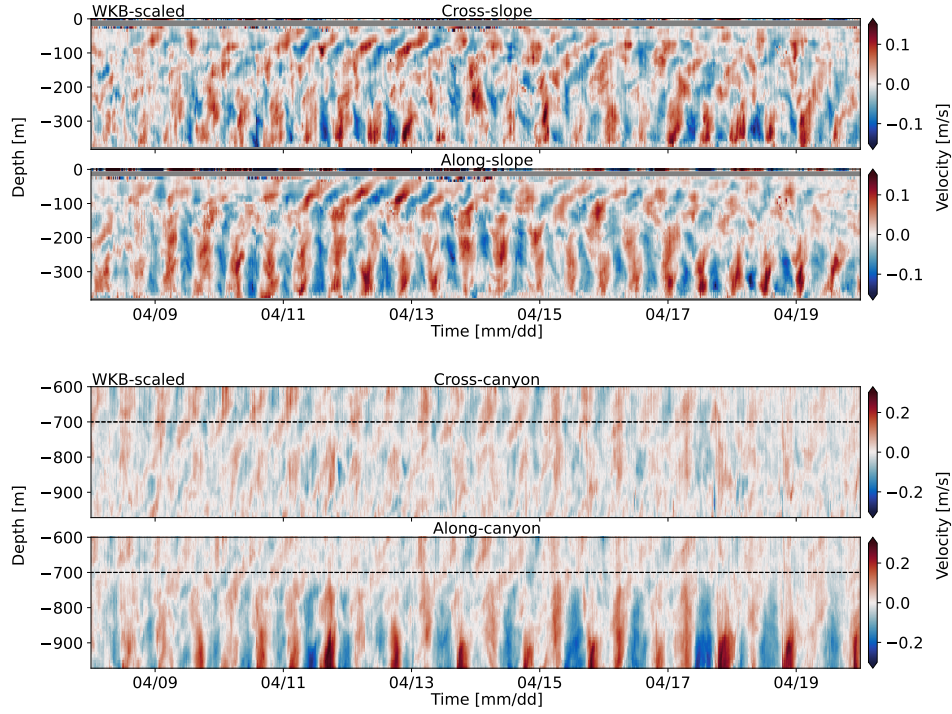


Figure 11. 40-hour high frequency WKB-scaled horizontal velocity data for Slope (top) and Axis (bottom), in April 2013. Components are separated as cross- (upper) and along-slope/canyon (lower). There are IW and IT of varied frequency, non-uniform vertical structure, and depth-dependence.

minimal (each line of the same colour is a different year), with annual spectra overlapping within the 95% confidence interval. The low-frequency sub-diurnal broadband ranges up to 1.00×10^{-5} Hz. The most defined spectral peaks are of the diurnal (1.16×10^{-5} Hz), NI (1.73×10^{-5} Hz), and semidiurnal (2.24×10^{-5} Hz) frequencies. Closely associated tidal constituents (such as S_2 and M_2) were identified in high frequency-resolution spectra (not shown) as having similar topographic and seasonal responses, and so are not resolved due to spectral averaging for ease of analysis; tidal constituents are therefore referred to generally (e.g. diurnal). The high-frequency IW continuum band ($7.00 \times 10^{-5} - 1.20 \times 10^{-4}$ Hz) ranges between M_6 ($\sim 6.8 \times 10^{-5}$ Hz) and the near- N spectral shoulder ($2.00 \times 10^{-4} - 1.00 \times 10^{-3}$ Hz).

At Slope, the sub-diurnal broadband is almost entirely along-slope (an energy ratio of up to 10:1, compared to cross-slope), with strength increasing inversely to frequency; the diurnal constituent is strongest cross-slope (over 3:1); the NI peak is equally distributed (1:1); and, the semidiurnal constituent is strongest along-slope (up to 2:1). The continuum is slightly stronger cross-slope, and

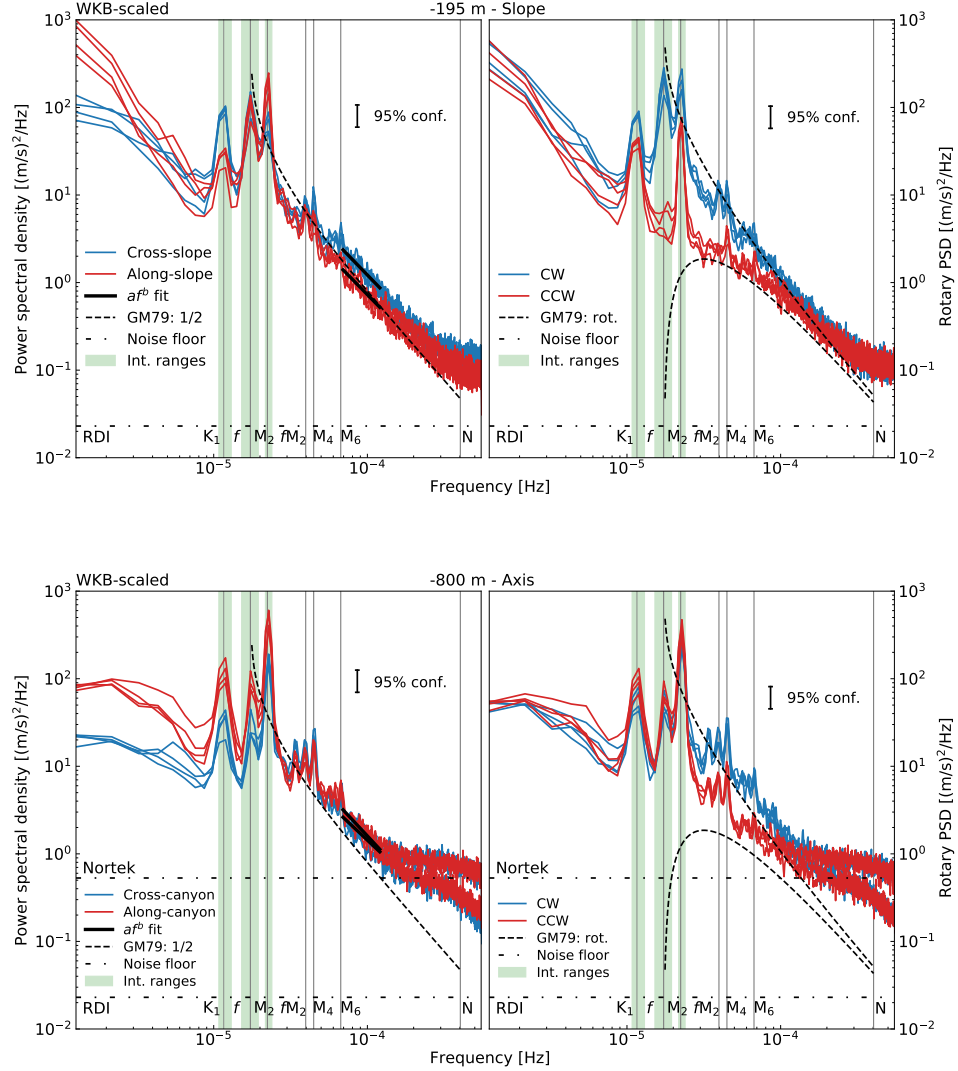


Figure 12. Mid-depth annual PSD (left) and rotary (right) spectra of WKB-scaled horizontal velocity data, for Slope (top) and Axis (bottom). Each line of the same colour is a different year. For PSD, cross- (blue) and along-slope/canyon (red) components are shown; for rotary, CW (blue) and CCW (red) components are shown. 95% confidence intervals are indicated by the black bar. Instrument noise floors (dotted line) and primary frequency constituents with integration range (vertical lines and green shading) are shown. For PSD, black lines indicate continuum power-law fit, and the dashed line is the GM79 spectrum (1/2 amplitude). For rotary, the GM79 spectrum is in rotary components (CW upper). Spectra at both sites are characteristically red, with prominent tidal and NI peaks.

455 trails off slightly whiter than the expected open-ocean GM slope of -2 (discussed in Section 5.2.5). Near N , a spectral shoulder is partially resolved as

457 a whitening effect, and is better observed in the raw (2-second) spectra (not
458 shown), discussed in Section 5.2.6. All bands are stronger in the CW rotary
459 component.

460 At Axis, compared to Slope, power is weaker at low frequencies below $4.00 \times$
461 10^{-6} Hz. Sub-tidal, tidal, and NI bands are all trend towards along-canyon
462 (from 3:1 at sub-diurnal, to 2:1 at semidiurnal, compared to cross-canyon), rec-
463 tilinear motions. Above the semidiurnal peak, the super-tidal and continuum
464 ranges are mostly CW (about 2:1), becoming rectilinear again approaching the
465 near- N spectral shoulder. The near- N spectral shoulder is more pronounced
466 at Axis in 2013 and 2014, seen below the Nortek 55 kHz noise floor which
467 masks the effect in 2017 and 2018 (discussed in Section 5.2.6).

468 5.1.3 Depth dependence

469 At each site, there is adjustment of spectral power near topography that is
470 frequency-dependent. The WKB-scaled PSD and rotary spectra were time-
471 averaged for annual 2D depth-frequency analysis (Figure 13). Results show a
472 general increase (or decrease, for NI at Slope) in spectral power (over an order
473 of magnitude) in a concentrated layer < a few hundred metres above bottom
474 (AB).

475 At Slope (Figure 13a), the sub-diurnal, tidal, and continuum bands show near-
476 slope intensification of IW energy. In contrast, the NI band is attenuated
477 near the slope, below an average depth of -250 m (130 m AB). Near-slope
478 adjustment is up to a factor of 10, compared to background energy. For the
479 broadband sub-diurnal range, intensification is mostly along-slope and CW.
480 The diurnal intensification is mostly along-slope and CCW. The NI near-slope
481 attenuation is entirely CW. The semidiurnal intensification is mostly along-
482 slope and strongly CW. Continuum intensification is mostly cross-slope and
483 CW.

484 At Axis (Figure 13b), most constituents show rectilinear, along-canyon near-
485 bottom intensification, below an average depth of -750 m depth (230 m AB).
486 Near-bottom adjustment is up to a factor of 100, compared to background
487 energy. The sub-diurnal, diurnal, and NI intensification is entirely along-
488 canyon, with little to no power in the cross-canyon direction. The NI band,
489 in contrast to Slope, has bottom-intensified flow that is almost entirely along-
490 canyon. The semidiurnal intensification is strongly along-canyon, but with a
491 medium-strength cross-canyon signal that is sharply attenuated below -900 m.
492 Continuum strength varies between cross- and along-canyon, and is mostly
493 CW.

494 A vertical scale analysis roughly agrees with the qualitative observations of

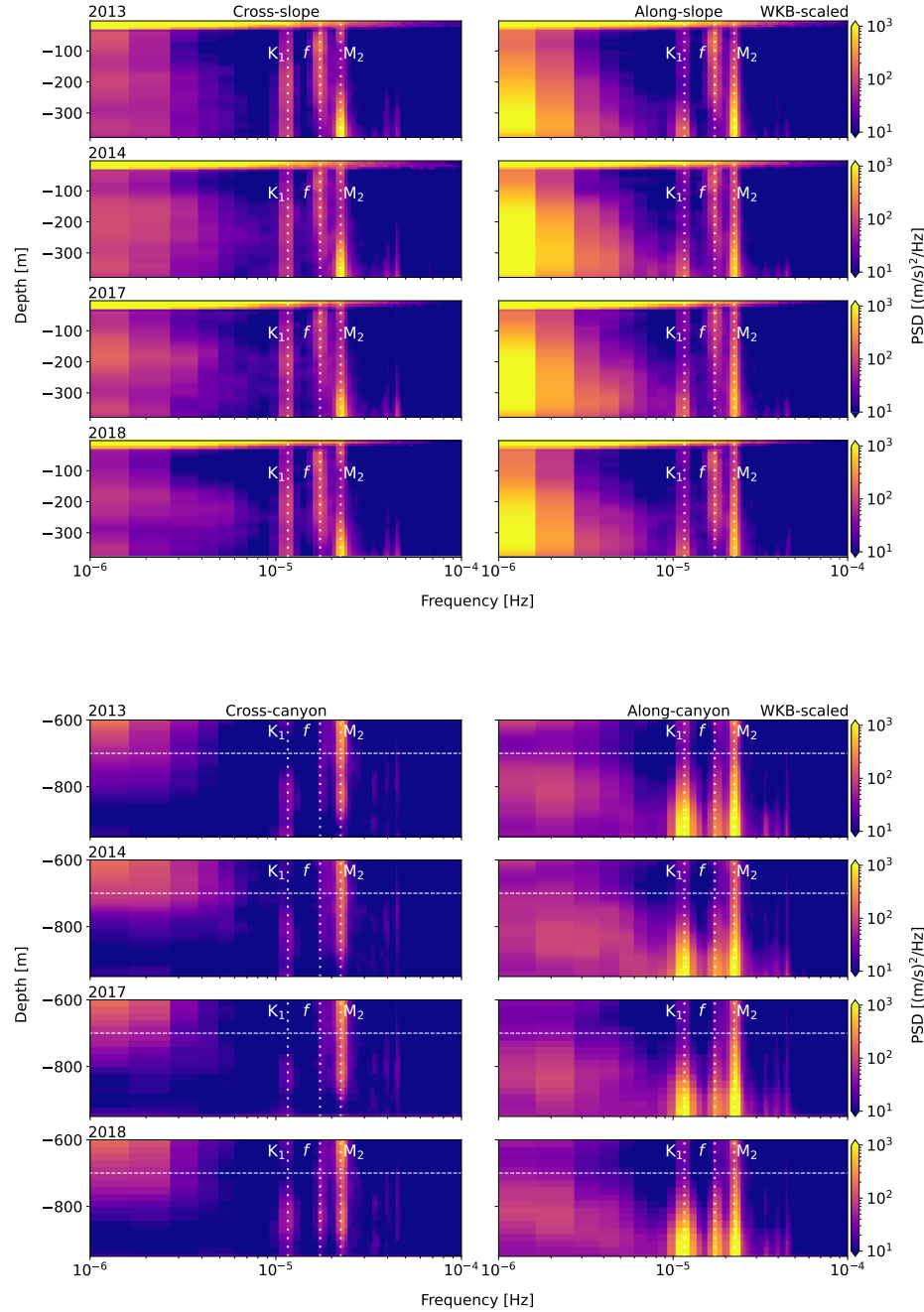


Figure 13. Depth-frequency PSD for Slope (top) and Axis (bottom). Components are separated as cross- (left) and along-slope/canyon (right). Determined from WKB-scaled horizontal velocity data. There is near-bottom intensification of individual frequency constituents (and near-bottom attenuation of the NI band, at Slope).

enhanced layer thickness. Gemmrich and Klymak (2015) found that mode-1 IW incident on sloped topography can induce a near-bottom turbulent flow layer, and that the vertical scale of the effect can be approximated as:

$$H \approx \frac{\pi U}{N} \quad (18)$$

where U is the forcing by horizontal velocity. For strong near-bottom velocities (Figure 11) and approximate buoyancy values (Figure 8) for near-topography depths at Slope ($U \approx 0.15$ m/s; $N \approx 3.5 \times 10^{-3}$ rad/s, at -350 m) and Axis ($U \approx 0.25$ m/s; $N \approx 2.5 \times 10^{-3}$ rad/s, at -900 m), estimates yield vertical scales of 135 m and 314 m, respectively. Results are similar to the qualitative thickness of 130 m AB at Slope, somewhat greater than the observed 230 m AB at Axis, and agree with the results of Gemmrich and Klymak (2015) for similar forcing and stratification. It should be noted that the CTD climatology data are from a nearby open-ocean site, and so do not reflect changes in stratification near topography.

5.2 Frequency-dependent response

There is frequency-dependent variability in the seasonality of the near-topography enhancement layer (and attenuation for NI at Slope). Little inter-annual variability is observed, noted only in the more intermittent sub-diurnal and NI seasonality. WKB-scaled PSD and rotary spectra were integrated over band-widths comprising each constituent's peak or frequency range (shown as shaded green in Figure 12), for each depth bin, yielding 2D estimates of depth-band power. Constituent frequency ranges are sub-diurnal ($\leq 1.08 \times 10^{-5}$ Hz), diurnal ($1.08 - 1.30 \times 10^{-5}$ Hz), NI ($1.52 - 1.95 \times 10^{-5}$ Hz), semidiurnal ($2.17 - 2.39 \times 10^{-5}$ Hz), continuum ($7.00 \times 10^{-5} - 1.20 \times 10^{-4}$ Hz), and shoulder ($2.00 \times 10^{-4} - 1.00 \times 10^{-3}$ Hz).

5.2.1 Sub-diurnal

At Slope, sub-diurnal ($\leq 1.08 \times 10^{-5}$ Hz) enhancement layer seasonality consists of intermittent pulses, strongest in fall and winter, and is one of few observations that is not inter-annually consistent (Figure 14a). At Axis, seasonality is weak, showing an occasional fall or winter pulse (Figure 14b). Seasonal forcing of the sub-diurnal constituent is inconclusive, as there is no correlation with wind, tides, or the expected low-frequency along-slope mean currents (Figure 9). Low-frequency flows can be affected by a variety of physical processes near slope, shelf, and canyon topography (Cummins, 2000), and a forcing analysis for the sub-diurnal range is left for further study.

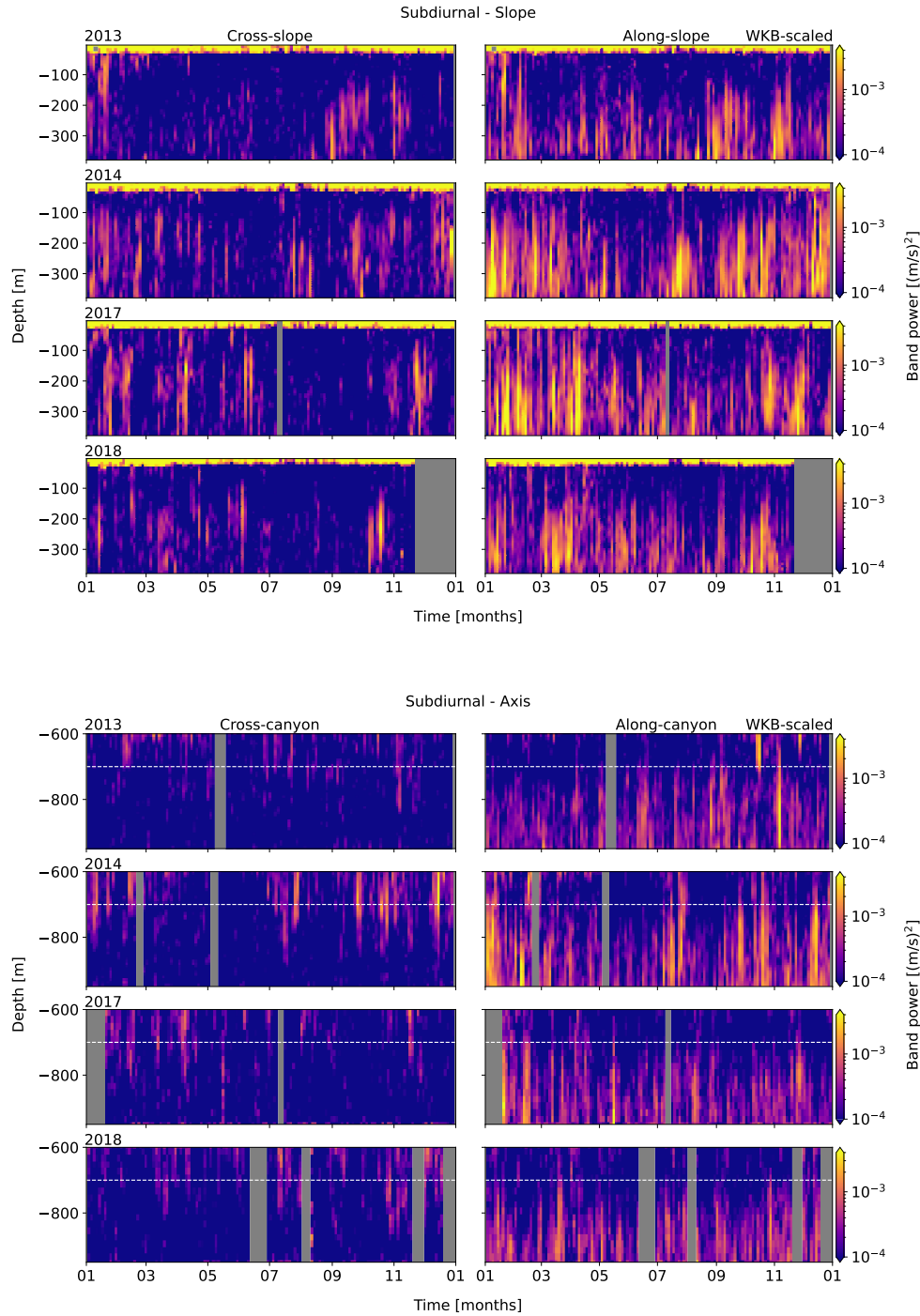


Figure 14. Band-integrated sub-diurnal PSD for Slope (upper) and Axis (lower), from WKB-scaled horizontal velocity data. Cross- (left) and along-slope/canyon (right) components are shown. Each row represents an analysis year, labelled at upper-left.

530 **5.2.2 Diurnal**

531 Diurnal ($1.08 - 1.30 \times 10^{-5}$ Hz) enhancement seasonality at Slope (Figure 15a)
532 is inter-annually consistent, with energy elevated late-spring through summer
533 (months 5-8) and again (weaker) in the fall/early-winter (months 11-1). Sea-
534 sonality at Axis is not readily apparent (Figure 15b).

535 The diurnal band is in sync with the local barotropic spring-neap cycle, fort-
536 nightily and seasonally, at both sites (Figure 16). Surface-level data were
537 obtained from the Canadian Hydrographic Service (CHS) operated gauge in
538 Tofino, approximately 90 km due north of Barkley Canyon, as hourly time-
539 series of deviation from chart datum, with power spectra diurnally band-passed
540 using the same process as for observations. Comparing long-term seasonal-
541 ity, the Tofino barotropic spring-neap amplitudes peak in months 6-8 and
542 11-2, corresponding well with the diurnal observations, and consistent inter-
543 annually. Fortnightly, 3-month phase-lag correlations were performed between
544 the depth-mean diurnal power and nearby surface level time series, for months
545 1-3, 4-6, 7-9, and 10-12, each year. Phase-lag correlations range from 0 to 1
546 day at Slope (inter-annual average of 0.5 days), and 0 to 2 days at Axis (inter-
547 annual average of 1.1 days) - both less than the time-resolution of the spectral
548 estimates (~ 2.7 days) used for correlations. It should be noted that Axis esti-
549 mates are only partial-depth and cannot fully resolve barotropic water-column
550 motions, potentially contributing to observed phase offsets. Regardless, the
551 diurnal observations are largely in sync with both the fortnightly and seasonal
552 local barotropic spring-neap cycle.

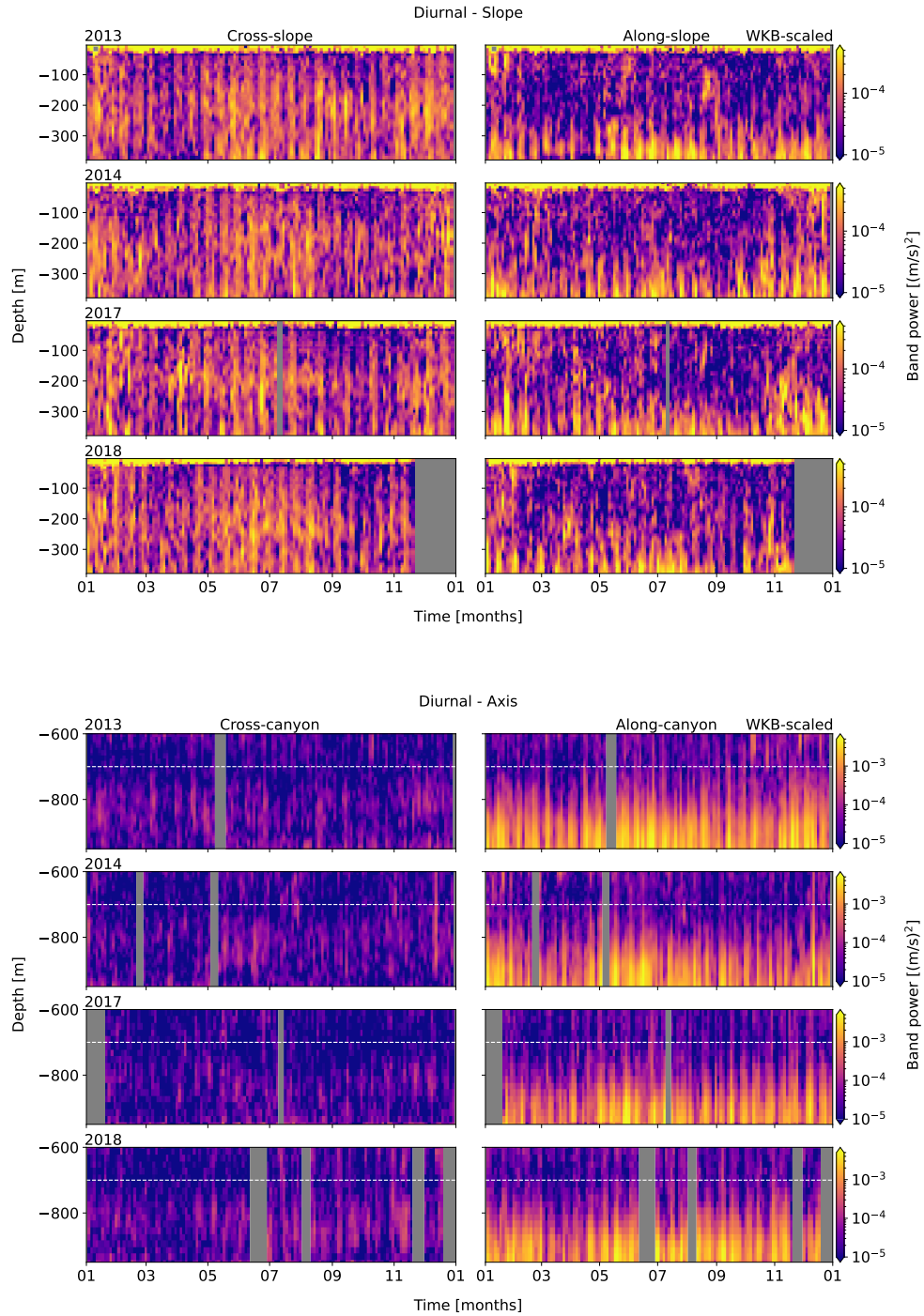


Figure 15. Band-integrated diurnal PSD for Slope (upper) and Axis (lower), from WKB-scaled horizontal velocity data. Cross- (left) and along-slope/canyon (right) components are shown. Each row represents an analysis year, labelled at upper-left.

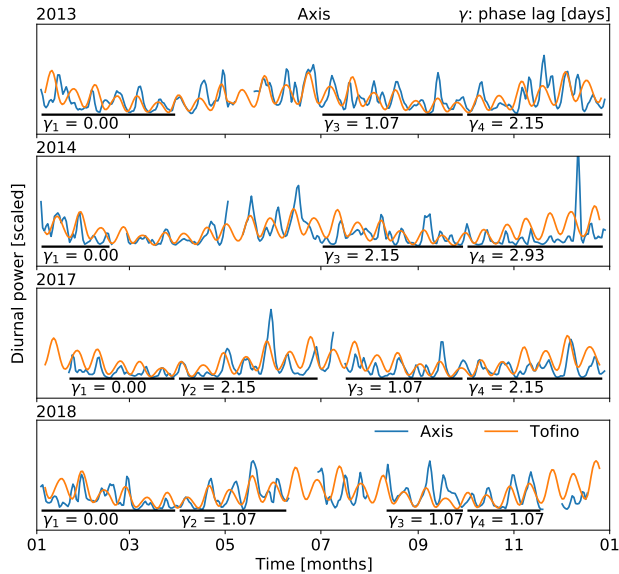
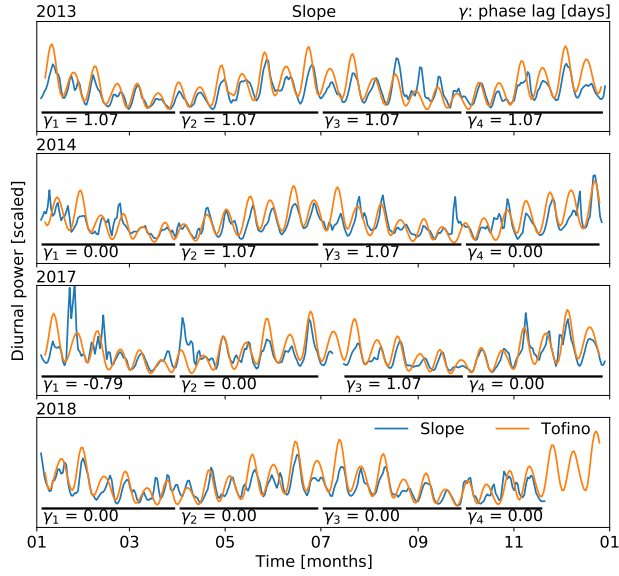


Figure 16. Diurnal barotropic forcing comparison. Phase-lag correlation and amplitude (scaled) comparisons for band-integrated power of diurnal surface level data (Tofino, orange) and WKB-scaled depth-mean diurnal power (blue) at Slope (top) and Axis (bottom). Black bars indicate seasonal correlation ranges. There is a consistent yet minor phase-lag, less than the time-scale of each spectral estimate.

553 **5.2.3 Near-inertial**

554 At Slope, NI ($1.52 - 1.95 \times 10^{-5}$ Hz) seasonality above the attenuation re-
555 gion is highly intermittent, with pulses occurring most likely in the fall and
556 early-winter, though possible year-round (Figure 17a). At Axis, generally only
557 significant fall and early-winter events from Slope are evident (Figure 17b).
558 Seasonality is inter-annually consistent, but specific events are not.

559 For prominent pulses at Slope, there are periods of downward propagation
560 of NI energy from the ML (above -50 m) to about -100 m, lasting up two
561 weeks, after which the deep response increases quickly. At Axis, the timing of
562 observed pulses appears to correspond to the delayed deep response at Slope.
563 Figure 18a shows a sample event in September, 2014. An event (likely wind,
564 to be discussed), deposits energy into the ML on September 3. Over the next
565 8 days, energy is transferred down to about -100 m. Upon reaching this depth,
566 there is an immediate deep response. Energy continues to pool around -100 m,
567 maintaining the deep response until September 14, when NI energy appears
568 to have dissipated. There are many of these events each year, enumerated in
569 Figure 19b. The fall sees the most events, all of which are short lived, from
570 7-9 days, while the winter has the longest events, up to 16-18 days.

571 Slab model results indicate NI forcing is qualitatively linked with regional wind
572 events in the fall and early-winter (Figure 20). Wind data were obtained from
573 the closest Fisheries and Oceans Canada (DFO) weather buoy, La Perouse
574 (46206, 50 km N), as time series of magnitude and direction. Regional season-
575 ally varying ML depth, H , is defined by Thomson and Fine (2003) and Li et
576 al. (2005) for nearby (35 km NW) Line P Station 3; the ML is thick in winter
577 and spring (down to about -60 m), and thinnest summer through early-fall
578 (up to about -20 m). There are large wind data gaps during later years (2014,
579 2017, and 2018), so 2013 is used as the sample year. Results for later years
580 are available in Appendix A (Section 8). Results yield time series of NI ML
581 currents exceeding 0.1 m/s that are qualitatively similar to wind data, most
582 notably in the fall and early-winter. However, not every event that shows up
583 in the ML is evident in the NI depth-band observations.

584 Seasonal slab model correlations with NI depth-band power suggest interior
585 NI response to wind forcing is strongest in summer and fall (not shown). To
586 better quantify wind forcing of NI depth-band power, seasonal correlations
587 were obtained similarly to diurnal spring-neap forcing. Correlation estimates
588 were initially poor; the apparent delay in the deep response may affect cor-
589 relation with the quicker slab response. To cope, a 2-month rolling average
590 was applied to each time-series and relaxed until correlations began to de-
591 volve. Ideal rolling average intervals were found to be 3-weeks for the slab

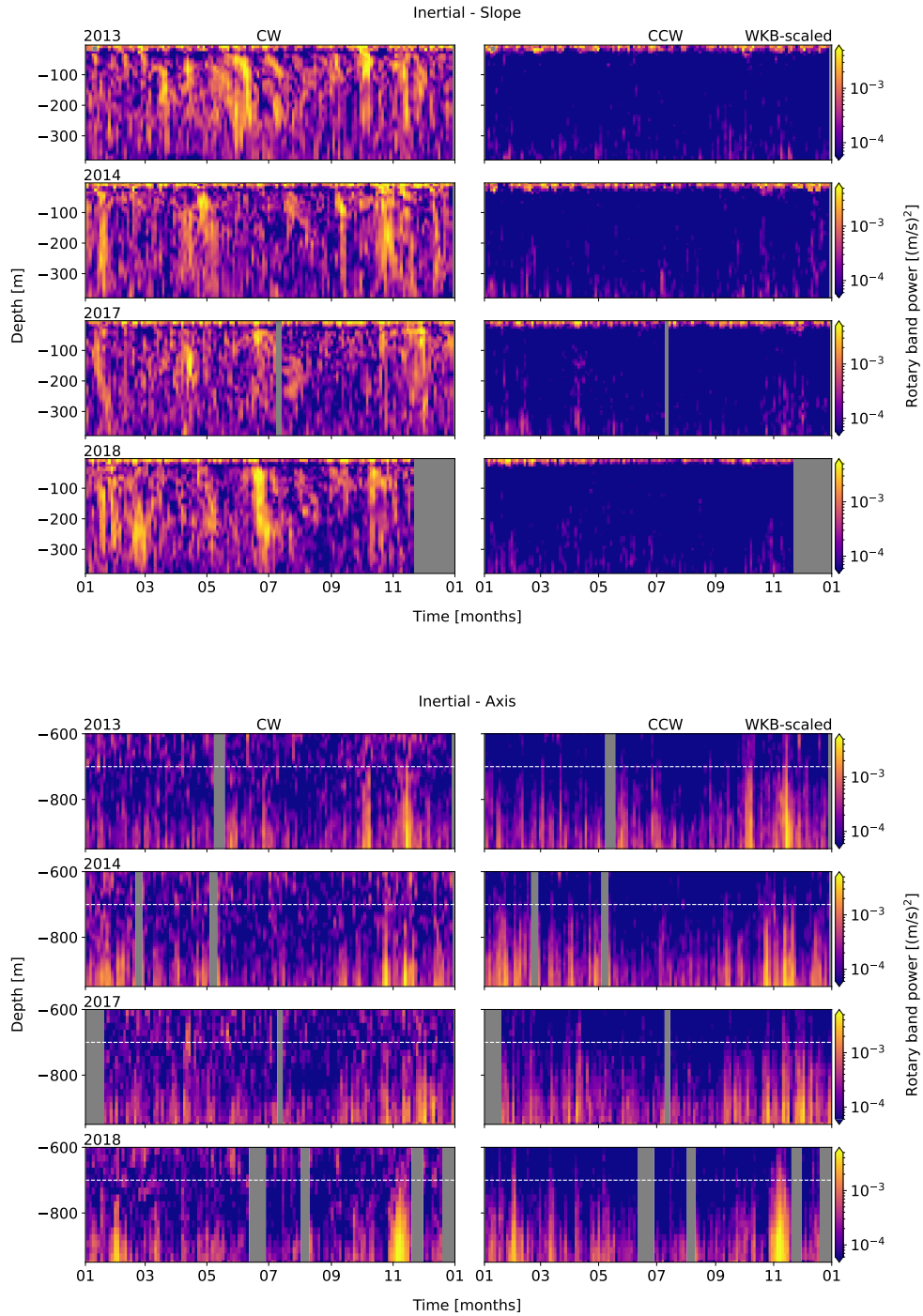


Figure 17. Band-integrated NI rotary PSD for Slope (upper) and Axis (lower), from WKB-scaled horizontal velocity data. CW (left) and CCW (right) components are shown. Each row represents an analysis year, labelled at upper-left.

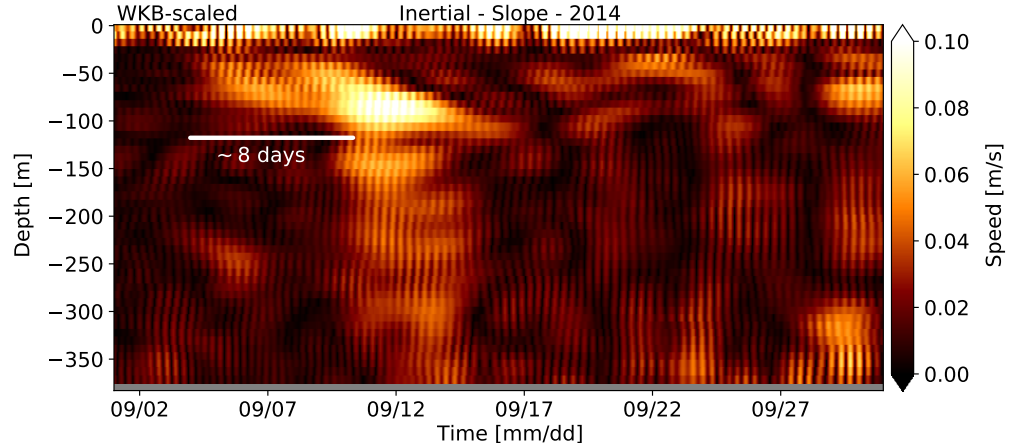


Figure 18. Transfer of NI energy in band-passed NI velocity (total) for September, 2014. A wind event excites NI energy in the ML around September 9. Energy is transferred down to about -100 m over about 8 days, after which there is a deep response.

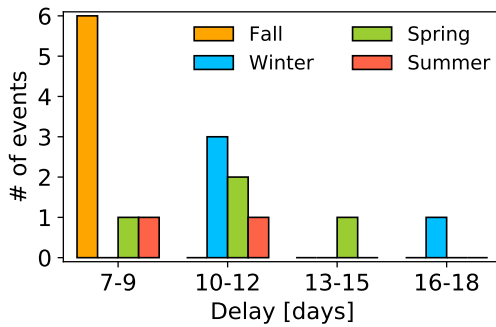


Figure 19. Histogram of delayed NI events. Delayed NI deep response events are most common and short-lived in the fall, least common in summer, and longest in the winter.

592 data, and 1-week for site observations, as the wind data were more highly
 593 variable to begin (not shown). At Slope, correlations are strong-positive in
 594 the fall, and weak- to medium-positive in summer. At Axis, correlations are
 595 strong-positive in summer, and weak- to medium-positive in fall. Seasonal cor-
 596 relations are otherwise inconsistent. The fall and summer correlation periods
 597 encompass notable wind events that occur while the ML is thin, and there is
 598 a more notable deep response.

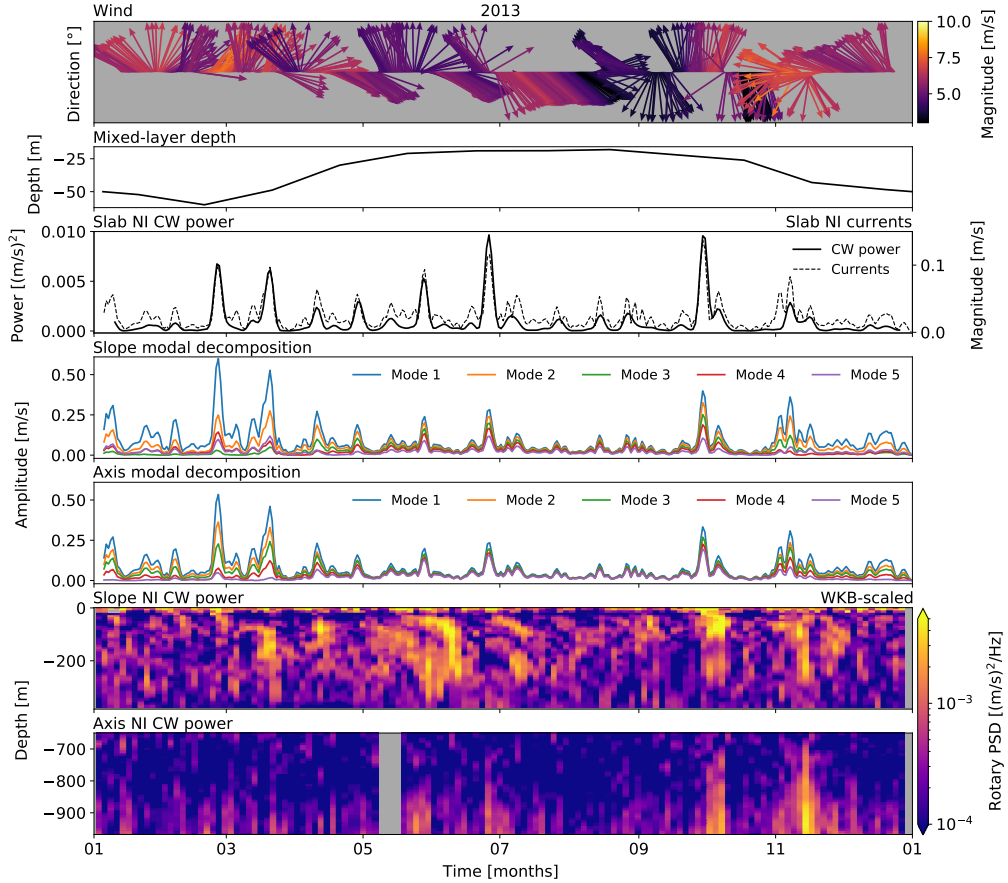


Figure 20. NI forcing analysis for 2013. Panels are (i) wind direction and amplitude, (ii) monthly-averaged ML depth for Line P station 3 as determined by Li et al. (2005), (iii) slab model NI CW power and NI currents, (iv, v) seasonal mode amplitudes for Slope and Axis, and (vi, vii) band-integrated NI CW power at Slope and Axis. There appears to be a complex relationship between the wind, ML, slab currents, and mode amplitudes in driving the NI observations, with the most obvious effects in the fall. Due to significant data gaps, plots for other analysis years are in Appendix A (8).

599 Seasonal vertical mode amplitudes suggest high-mode contributions lead to
 600 greater NI deep response (Figure 21). For NI IW generation by the NI ML
 601 currents, the stratification-dependent vertical mode structure is determined as
 602 described in Section 3. When the ML is thin, contributions from low modes (1
 603 and 2) and high modes (3, 4, 5) are about equal ($\sim 52\%$ low modes); when the
 604 ML is thick, modes 1 and 2 dominate ($\sim 74\%$). Similar to the slab correlations,
 605 there is a greater deep response when the ML is thin and higher modes are
 606 equal contributors, such as in the early-fall when strong storms begin to arrive.

607 High modes contribute most in the summer when the ML is thinnest, though
 608 there are few storms this time of year; however, even weak summer wind events
 609 occasionally warrant a deep response. In contrast, there are many strong wind
 610 events in winter and spring when the ML is thick and low modes dominate,
 611 but there is often little or no deep response. A deep response associated
 612 with high-mode NI IW is not unexpected, though is somewhat misunderstood
 613 (Gill, 1984; Zervakis & Levine, 1995; Alford, 2003); though low-modes tend
 614 to dominate NI IW energy they largely propagate laterally, while high-mode
 615 energy radiates downward and equatorward (Alford et al., 2016).

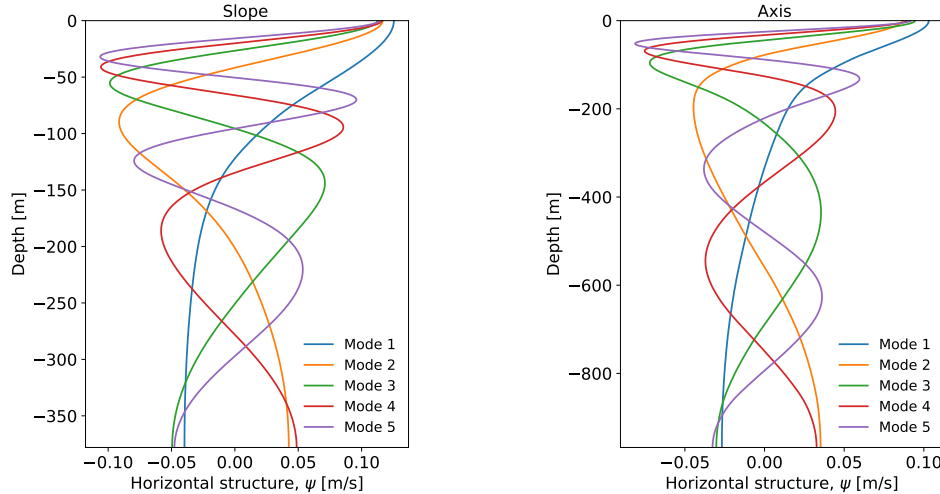


Figure 21. Vertical mode decomposition. Depth-dependent horizontal structure of mode amplitudes, for Slope (left) and Axis (right). Mode structure is dependent on site depth and the local stratification profile.

616 5.2.4 Semidiurnal

617 Semidiurnal ($2.17 - 2.39 \times 10^{-5}$ Hz) enhancement layer seasonality at Slope
 618 is inter-annually consistent and subtle, showing a slight pulse that begins in
 619 the late-spring/early-summer (months 4/5) and an even weaker pulse in the
 620 fall/early-winter (Figure 22a). Seasonality at Axis is not readily apparent
 621 (Figure 22b).

622 Semidiurnal barotropic spring-neap forcing is intermittently in-and-out of phase,
 623 at both sites, suggesting some remote baroclinic forcing (Figure 23). Phase-lag
 624 correlations were determined as for the diurnal band. The scaled semidiurnal
 625 depth-mean band-power amplitudes vary greatly from the seasonal spring-neap
 626 surface levels. Fortnightly phase-lags are inconsistent, and for 3-month periods
 627 range from 0 to 4 days at Slope (inter-annual average of 2.3 days), and from

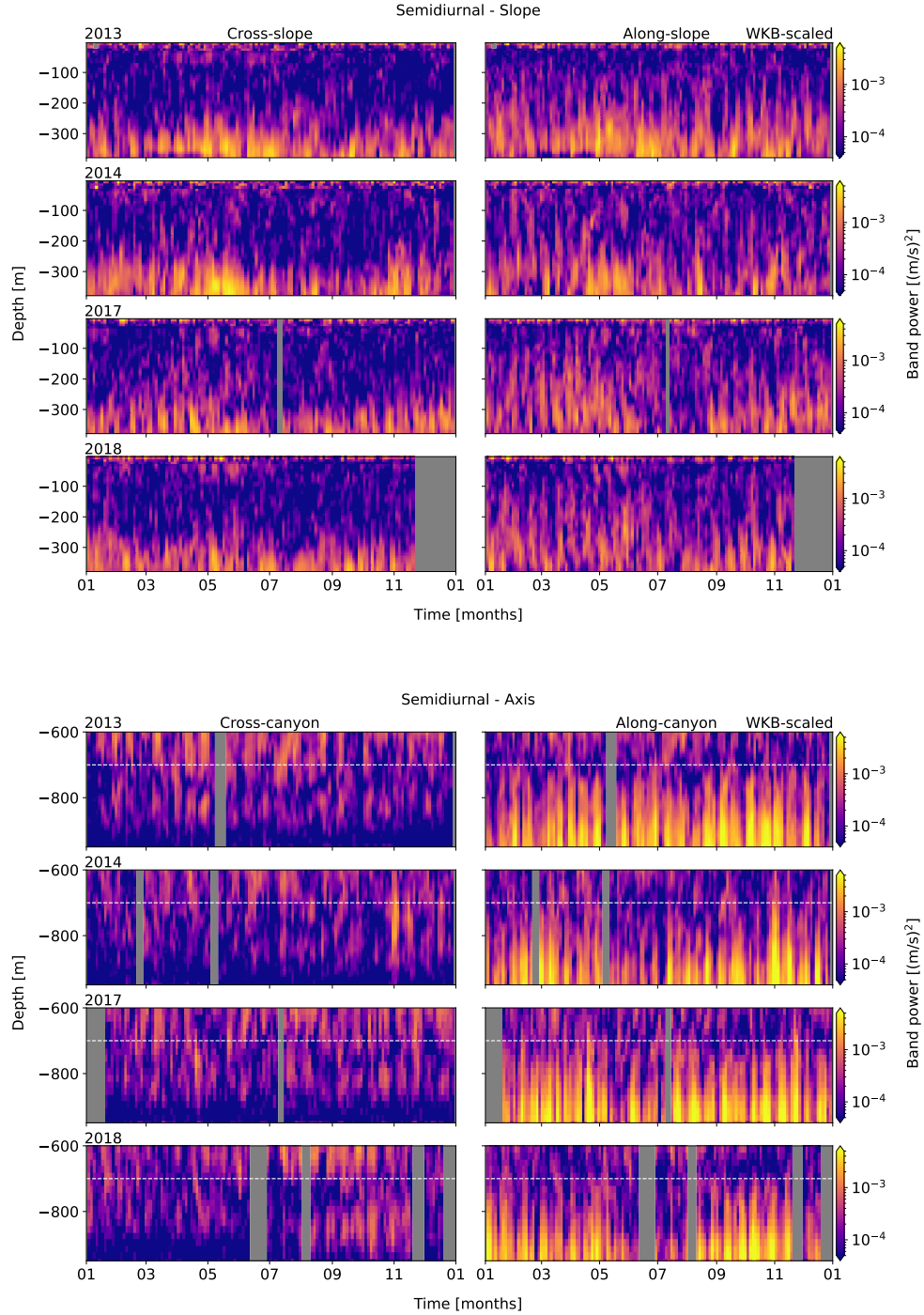


Figure 22. Band-integrated semidiurnal PSD for Slope (upper) and Axis (lower), from WKB-scaled horizontal velocity data. Cross- (left) and along-slope/canyon (right) components are shown. Each row represents an analysis year, labelled at upper-left.

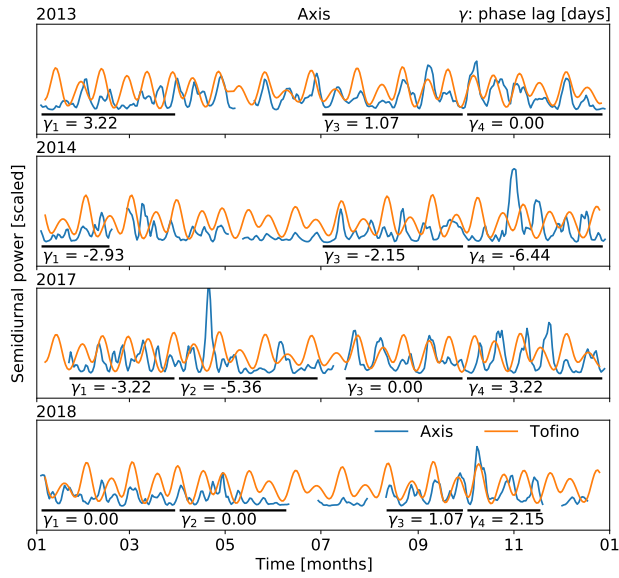
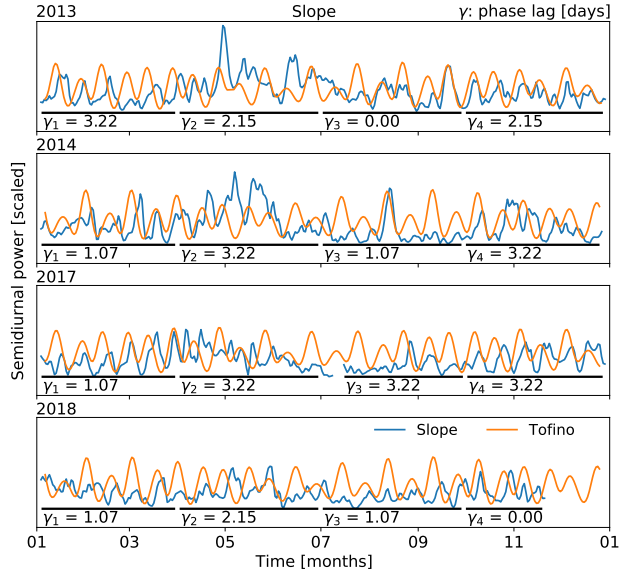


Figure 23. Semidiurnal barotropic forcing comparison. Phase and amplitude (scaled) comparisons for band-integrated power of semidiurnal surface level data (Tofino, orange) and WKB-scaled depth-mean semidiurnal power (blue) at Slope (top) and Axis (bottom). Black bars indicate seasonal correlation ranges. Though the instrument amplitude is highly irregular, there is a variable phase lag that suggests a mix of local barotropic and remote baroclinic forcing.

628 0 to 6 days at Axis (inter-annual average of 2.8 days). The irregularity of the

629 phase-offset suggests a mix of local barotropic and remote baroclinic forcing.

630 5.2.5 Continuum

631 Seasonality of IW continuum energy ($7.00 \times 10^{-5} - 1.20 \times 10^{-4}$ Hz) at Slope
 632 is inter-annually consistent, heightened in spring through early-summer, and
 633 again through the fall (Figure 24a). At Axis, seasonality is less apparent,
 634 though there is generally more activity in the fall (Figure 24b).

635 At both sites, the observed continuum amplitude is higher, and the spectral
 636 slope more negative, as compared to the open-ocean GM spectrum (Figure
 637 25). For near-bottom depth-specific time series of WKB-scaled PSD (Slope
 638 -300 m; Axis -900 m), a power law of af^b was fit to the continuum frequency
 639 range and smoothed in two week intervals, resulting in a time series of power
 640 law amplitude (a) and slope (b). A similar fit was applied to the open-ocean
 641 GM spectrum (its energy halved to compare with u and v components), to find
 642 $a_{GM,0.5} \approx 2.7 \times 10^{-9} \text{ m}^2\text{s}^{-2}\text{Hz}^{-1}$ and $b_{GM,0.5} \approx -2.1$. At both sites, observed
 643 a ranges within $2 - 5 \times 10^{-9} \text{ m}^2\text{s}^{-2}\text{Hz}^{-1}$, and b within -2.0 – -2.3, similar
 644 but generally higher than open-ocean GM values. Time series of power law
 645 amplitude and slope are strongly correlated, each a rough copy of depth-mean
 646 continuum depth-band power seasonality (not shown).

647 Elevated near-topography continuum energy leads to enhanced dissipation
 648 rates, ε , at both sites (Figure 26). WKB-scaled continuum energy was 'whitened'
 649 over the continuum frequency range - its power multiplied by f^2 - then av-
 650 eraged to find mean continuum energy, E_c , in depth and time. Determined
 651 similarly, a mean value of open-ocean GM energy was found to be $E_{GM} \approx$
 652 $8.1 \times 10^{-9} \text{ m}^2\text{s}^{-2}\text{Hz}$. The ratio of E_c/E_{GM} yields non-isotropic E_c amplitudes
 653 up to $7 \times E_{GM}$ near topography, while away from topography E_c levels fall to
 654 equal or below that of E_{GM} (not shown). From IW interaction theory (Althaus
 655 et al., 2003), dissipation estimates were calculated from the WKB-scaled E_c
 656 fits as:

$$657 \quad \varepsilon = \varepsilon_0 \frac{N_0^2}{N_{GM}^2} \frac{\langle E_c^2 \rangle^2}{\langle E_{GM}^2 \rangle^2} f(R_\omega) \quad (19)$$

658 where $\varepsilon_0 = 4.1 \times 10^{-11} \text{ W/kg}$, $\langle E_c^2 \rangle^2 / \langle E_{GM}^2 \rangle^2$ is the measured ratio of con-
 659 tinuum energy to GM energy over the same frequency range, and the upper
 660 bound

$$661 \quad f(R_\omega) = \left(\frac{R_\omega + 1}{R_\omega} \right)^2 \left[\cosh^{-1} \left(\frac{N_0}{f} \right) + \frac{25 \cos^{-1}(f/N_0)}{\sqrt{R_\omega}} \right] \quad (20)$$

662 is an energy ratio as defined by Sun and Kunze (1999), with $R_\omega = 2.13$ (Kunze
 663 et al., 2002) for a continuum with predominantly semidiurnal forcing (to be
 664 discussed). Results exceed 10^{-8} W/kg near topography, fluctuating with con-
 665 tinuum energy seasonality. Away from topography, dissipation is on the order

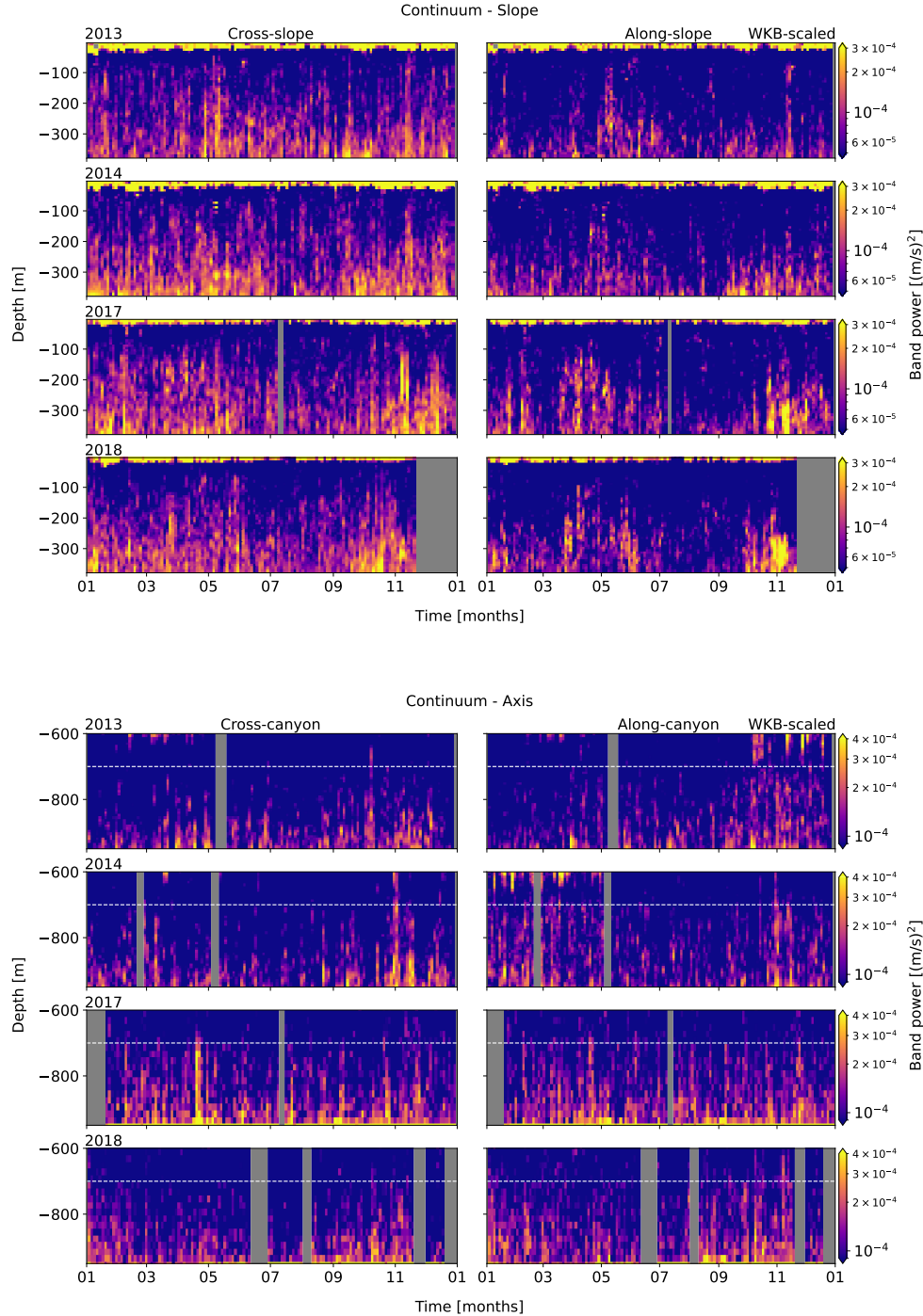


Figure 24. Band-integrated continuum PSD for Slope (upper) and Axis (lower), from WKB-scaled horizontal velocity data. Cross- (left) and along-slope/canyon (right) components are shown. Each row represents an analysis year, labelled at upper-left.

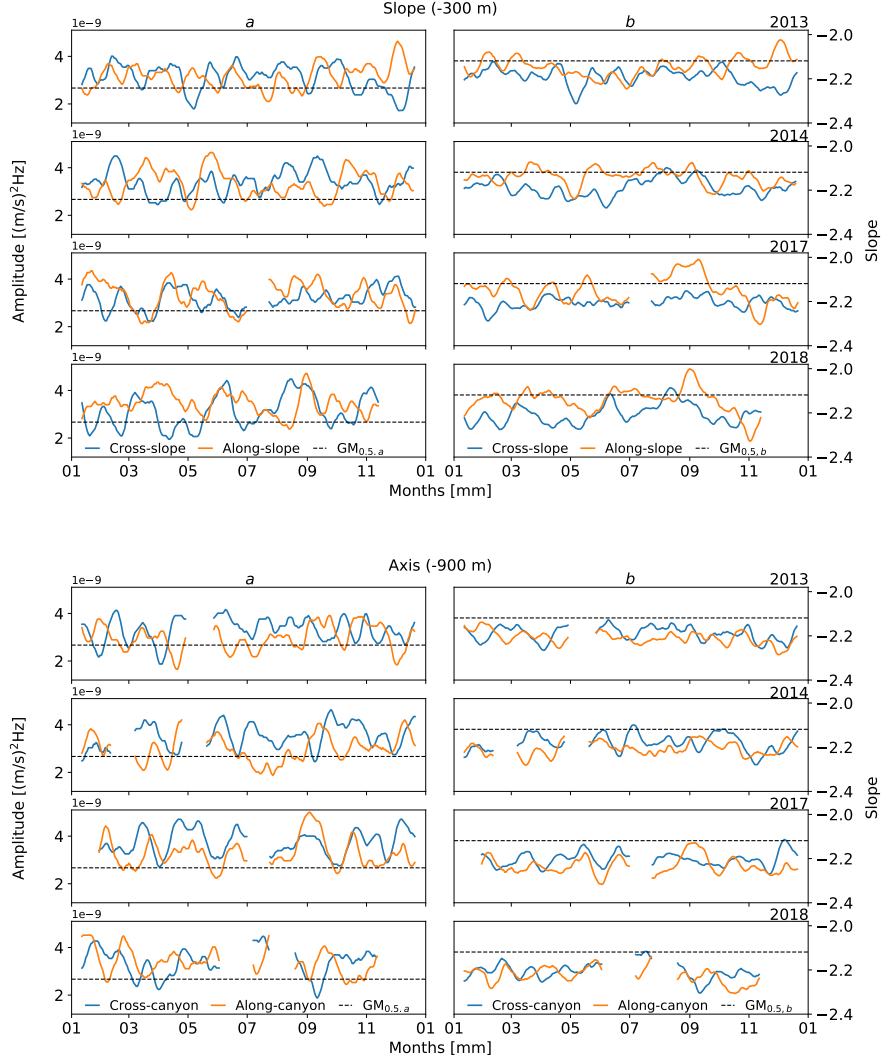


Figure 25. Time-series of continuum power law fits. Continuum amplitude, a (left), and slope, b (right), of power law ($a f^b$) fits to lower-depth WKB-scaled PSD, at Slope (top) and Axis (bottom). For each site, each row is a year, labelled upper-right. Time series were smoothed over two weeks. Compared to GM, amplitudes are elevated up to $2 \times$ GM in the centre of the enhancement layer, with slopes down to -2.3.

of 10^{-9} W/kg or less. Turbulent eddy diffusivities, κ , are similarly elevated near topography (Figure 26). From ϵ , diffusivity was calculated as by Kunze et al. (2002), as:

$$\kappa = \frac{\gamma \epsilon}{N_0^2} \quad (21)$$

where $\gamma = 0.2$ is the mixing efficiency for high-Reynolds-number turbulence.

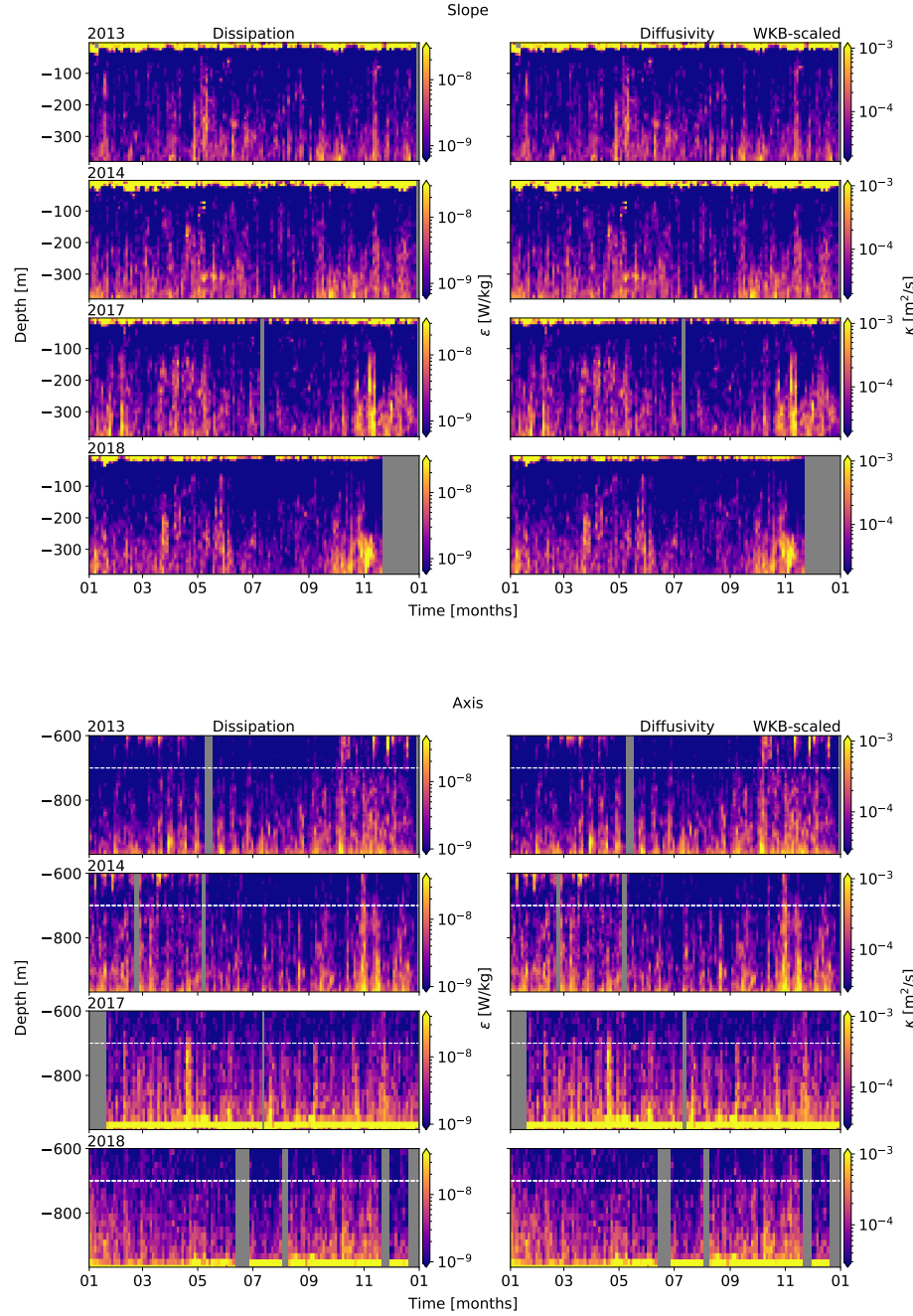


Figure 26. Dissipation rates (left) and turbulent eddy diffusivity (right), for WKB-scaled horizontal velocity spectra at Slope (top) and Axis (bottom). Both dissipation and diffusivity are heightened near topography.

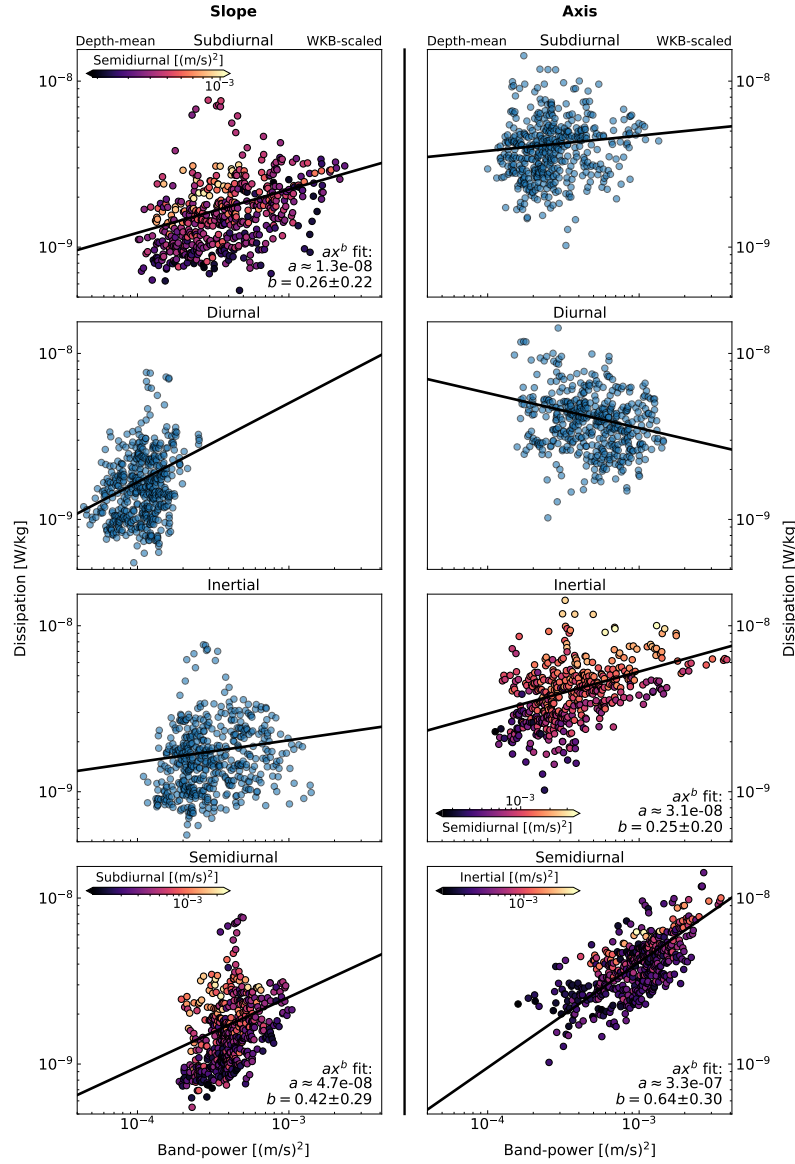


Figure 27. Dissipation power law fits. Scatter plots are for depth-mean WKB-scaled depth-band power at Slope (left) and Axis (right), all years. Frequency constituents are listed for each row, as sub-diurnal (top), diurnal (second), NI (third), and semidiurnal (bottom). Black lines indicate the power law fit, listed in the lower-right of each frame. For each site, the two most likely contributors are coloured by the strength of the other.

671 Turbulent eddy diffusivities reach $10^{-3} \text{ m}^2\text{s}^{-1}$ near topography, again fluctuating
672 with continuum energy seasonality. Away from topography, diffusivity
673 values are on the order of $10^{-5} \text{ m}^2\text{s}^{-1}$ or less, consistent with open-ocean values
674 (Gregg, 1989; Kunze et al., 2002).

675 Dissipation seasonality (derived from continuum energy seasonality) is cor-
676 related with semidiurnal forcing at both sites, with secondary contributions
677 from the sub-diurnal band at Slope, and the NI band at Axis (Figure 27). Dis-
678 sipation seasonality correlations were determined as for NI wind forcing, for
679 each constituent (not shown). At Slope, the semidiurnal band shows moderate
680 correlations throughout the year, and strong correlations in the spring, while
681 the sub-diurnal band shows weak to moderate correlations in both winter and
682 spring. At Axis, the semidiurnal band is strongly correlated all year, while
683 the NI band is moderate to strongly correlated in the spring and fall. There is
684 no apparent fortnightly modulation of continuum energy or vertical scale as-
685 sociated with diurnal or semidiurnal spring-neap effects. To further quantify
686 these relationships, power laws of ax^b were fit to scatter plots of depth-mean
687 dissipation-power time series for each frequency constituent. The process was
688 bootstrapped for improved uncertainties. At both sites the semidiurnal band
689 shows the best fit, and is stronger at Axis. The sub-diurnal band at Slope, and
690 the NI band at Axis, are secondary contributors with less obvious fits. Both
691 the semidiurnal and secondary bands contribute to higher dissipation as they
692 increase, but they do not drive each other. The power law fits for semidiurnal
693 driven dissipation are $\epsilon \sim M_2^{0.42 \pm 0.29}$ at Slope, and $\epsilon \sim M_2^{0.64 \pm 0.30}$ at Axis.

694 Multi-variate analysis improves power law fits, reinforcing the importance of
695 the secondary contributing constituents (Figure 28). Secondary constituents
696 were added to the semidiurnal power law fits as $ax_1^b + cx_2^d$, where x_1 is the depth-
697 mean semidiurnal band-power and x_2 is the secondary contributing band. The
698 process was bootstrapped for improved uncertainties. Multi-variate power laws
699 relationships of $\epsilon \sim M_2^{0.83 \pm 0.17} + \text{Sub}_{K1}^{0.59 \pm 0.13}$ and $\epsilon \sim M_2^{1.47 \pm 0.48} + \text{NI}^{0.24 \pm 0.06}$
700 were found for Slope and Axis, respectively. At Slope, the purely semidiurnal
701 fits are generally overestimated, and conservative in periods of high and low
702 dissipation, while multi-variate fits are less conservative and better reflect sea-
703 sonal variability. At Axis, purely semidiurnal fits are reasonable, but generally
704 underestimate dissipation in 2017 and 2018, while multi-variate fits are fairly
705 accurate in all years. A percent-good metric indicates the multi-variate fit is
706 closer to ϵ for 68% of data points at Slope, and 62% at Axis.

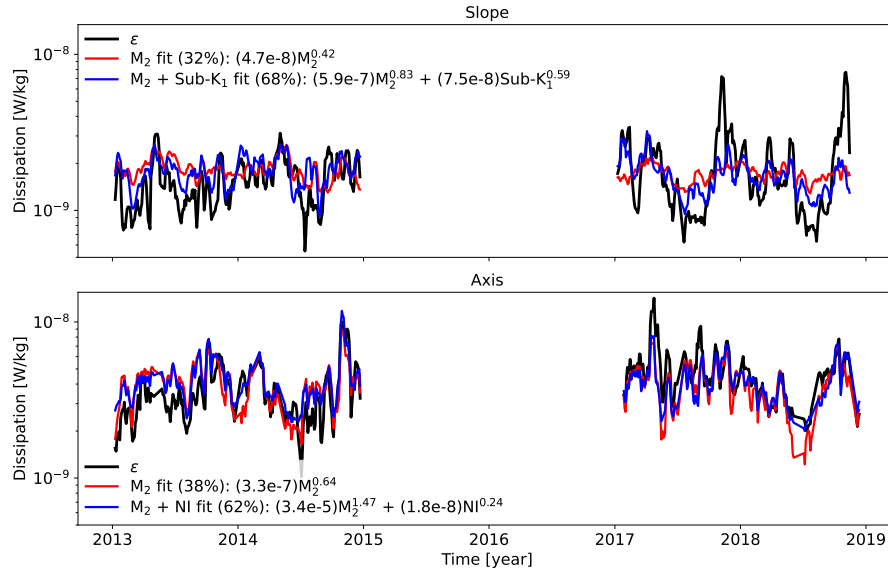


Figure 28. Dissipation multi-variate power law fits for Slope (top) and Axis (bottom). Comparison time series of depth-mean WKB-scaled dissipation (black), semidiurnal power law fits (red), and multi-variate power law fits (blue). Percent good is listed for each fit, as a measure of which fit line is closest to ϵ at each time step. Dissipation (black) time-series shows the seasonal trend towards a summer lull, with more energetic fall events in later years. The purely semidiurnal fits (red) are conservative in estimating periods of high and low energy, at Slope, and often underestimate at Axis. The multi-variate fits (blue) are improved, less conservative in estimating extremes at Slope, and fairly accurate at Axis.

707 5.2.6 Shoulder

708 The near- N spectral shoulder (here defined between $2.00 \times 10^{-4} - 1.00 \times 10^{-3}$
 709 Hz) is typically unresolved in oceanographic power spectra, and the 15-minute
 710 data used in this study only partly expose this feature. To properly analyse
 711 the shoulder, 2-second data from the 75 kHz RDI instruments were obtained to
 712 allow for increased Nyquist frequency. The data for this high-frequency range
 713 were then processed similarly to the other frequency constituents. Shoulder
 714 depth-band power is elevated near topography, though less uniformly than for
 715 lower-frequency constituents (Figure 29). At Slope, shoulder power is mostly
 716 cross-slope and rectilinear, and somewhat intermittent in its depth-dependent
 717 enhancement. At Axis, shoulder power is isotropic, and its depth-dependent
 718 enhancement more vertically uniform than at Slope. Shoulder power season-
 719 ality at Slope is subtle, somewhat heightened in the spring and fall, with
 720 intermittent brief pulses that are inconsistent in both depth and time. At
 721 Axis, there is subtly increased energy in the fall.

722 However, there are multiple issues with interpreting shoulder power seasonal-
 723 ity at Axis. During 2013 and 2014, there were adjustments to ADCP beam

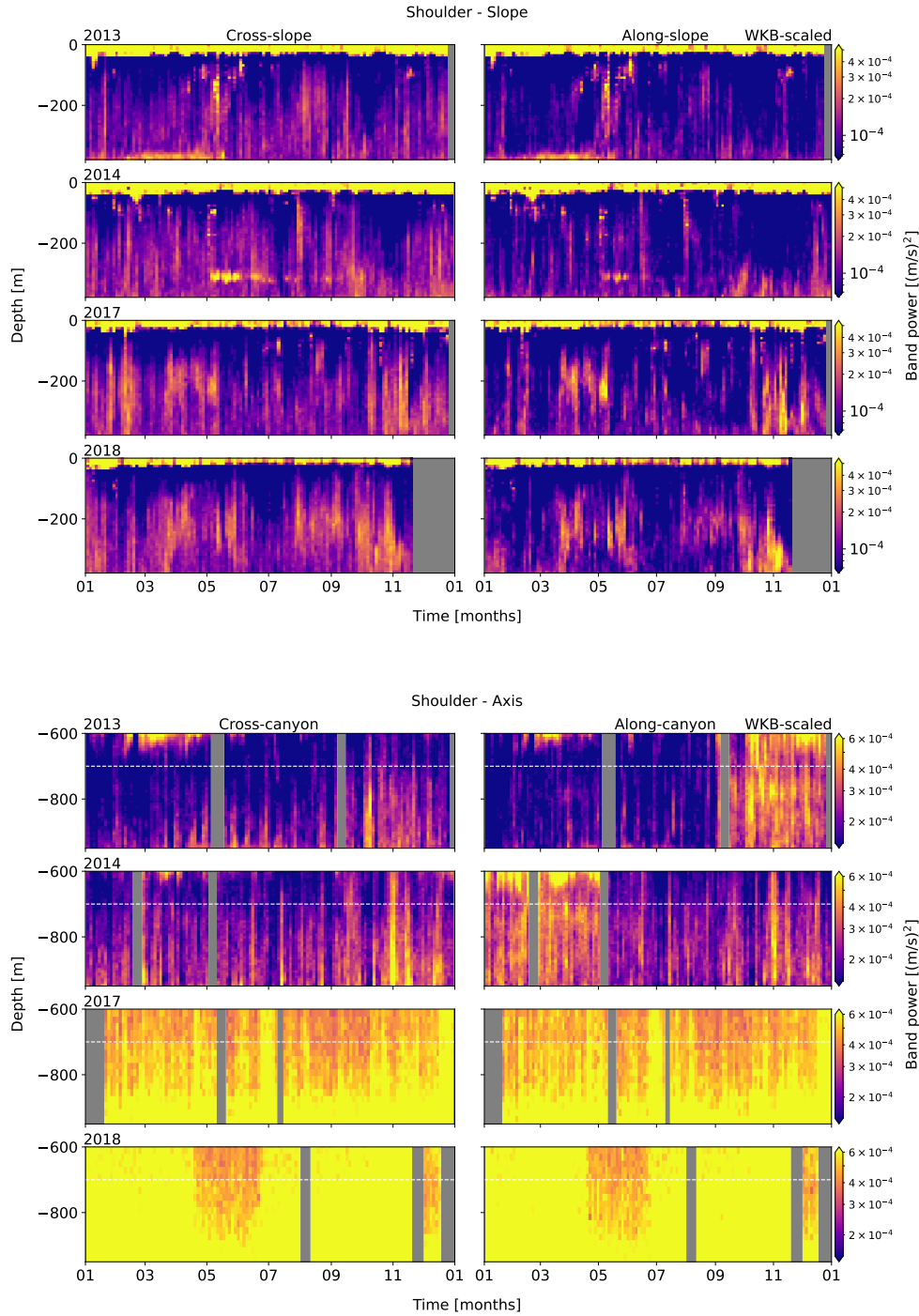


Figure 29. Band-integrated shoulder PSD for Slope (upper) and Axis (lower), from WKB-scaled horizontal velocity data. Cross- (left) and along-slope/canyon (right) components are shown. Each row represents an analysis year, labelled at upper-left.

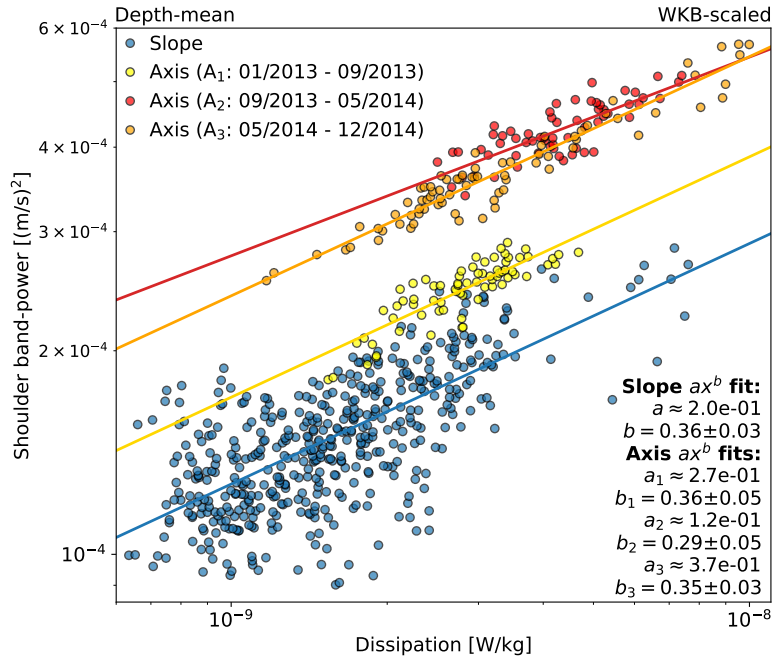


Figure 30. Power law relationship between dissipation and the spectral shoulder. Inter-annual depth-mean scatter plot for WKB-scaled dissipation and shoulder depth-band power, for Slope (blue) and Axis (yellow, red, orange). Slope data is for all four analysis years. Axis data is separated into three variance periods determined by instrument swaps and adjustments, for 2013 and 2014. All power law slopes agree within uncertainty, suggesting strong correlation to dissipation that does not depend on site topography.

724 orientation (2013/05 and 2014/05) relative to canyon topography, an instru-
 725 ment swap (2014/05), and a switch from 4- to 3-beam solutions (2013/05),
 726 somehow resulting in distinct periods of higher variance (though this did not
 727 affect lower frequencies, likely due to their broader horizontal scale). These
 728 periods are defined as: A₁ (2013/01 - 2013/09), while the first RDI 75 kHz in-
 729 strument was operating with a 4-beam solution; A₂ (2013/09 - 2014/05), after
 730 the same instrument was adjusted to a 3-beam solution, showing heightened
 731 variance up to 3× A₁; and A₃ (2014/05 - 2014/12), after a new 75 kHz 3-beam
 732 instrument was swapped in, and variance was lowered to up to 2× A₁. It is
 733 possible that the difference between A₂ and A₃ could be physical, as there is
 734 a coinciding drop in continuum energy; possible only if continuum energy is
 735 not (or at least not as much) affected by the instrument adjustments, which
 736 seems to be indicated in the comparative variance of raw spectra. When an
 737 orientation adjustment coincided with a variance jump (as in 2014/05), the
 738 rotation was minimal (up to ∼20°), suggesting the wave field would have to be

739 quite asymmetric to result in such a difference; this is unlikely. In 2017 and
740 2018, use of Nortek 55 kHz instruments at Axis does not allow for clear res-
741 olution of the spectral shoulder, as those instruments' noise floors are higher
742 than that of the previous 75 kHz ADCPs (Figure 12). Re-evaluation of the
743 spectral shoulder variance at Axis is worthwhile, but beyond the scope of this
744 study.

745 There is a distinct power law relationship between dissipation and the spectral
746 shoulder (Figure 30). Power law fits for WKB-scaled depth-mean dissipation
747 and shoulder depth-band power (P_{Sh}) were determined as for the continuum
748 analysis of Section 5.2.5. At Slope, there is a reasonable fit of $P_{sh} \sim \epsilon^{0.36} \pm 0.03$
749 for all four years. At Axis, a power law was fit to each of the three variance
750 periods in 2013 and 2014. Though amplitudes vary between periods, power law
751 slopes are similar, with $P_{Sh} \sim \epsilon^{0.36 \pm 0.05}$, $P_{Sh} \sim \epsilon^{0.29 \pm 0.05}$, and $P_{Sh} \sim \epsilon^{0.35 \pm 0.03}$
752 for periods A₁, A₂, and A₃, respectively. Power law slopes at both Slope and
753 Axis all agree within uncertainty (averaging $P_{Sh} \sim \epsilon^{0.34 \pm 0.08}$), suggesting a
754 strong connection between spectral shoulder energy and turbulence that does
755 not depend on site topography.

756 6 Discussion

757 6.1 Canyon axis mean currents

758 The periodic (~ week) up-canyon shoaling mean flow at Axis (between -
759 700 and -900 m), with its underlying near-bottom down-canyon layer, is no-
760 table for its seasonal and inter-annual consistency and circulation implications
761 (close to zero net mean flow), important for understanding sediment transport
762 and physical-biological coupling influencing VICS productivity (Xu & Noble,
763 2009). In previous biological studies at Barkley Canyon (Cabrera et. al, 2018;
764 Chauvet et al., 2018), a two-layer flow system was noted similar to that of
765 Hudson Canyon (Hotchkiss & Wunsch, 1982) and Monterey Canyon (Xu &
766 Noble, 2009); the systems were attributed to circulation cells caused by along-
767 canyon pressure gradients driven by consistent large-scale quasi-geostrophic
768 along-shelf regional currents, similar to those observed at Slope. The shoal-
769 ing of these currents was observed with periodicity ranging from semidiurnal
770 (Monterey Canyon) to > than a few days (Hudson Canyon), and found to shoal
771 at an angle similar to that of the up-slope gradient (Hotchkiss & Wunsch, 1982;
772 Petrunio et al., 1998; Xu & Noble, 2009). Tidal rectification, where tides force
773 an up-slope pressure gradient (Garrett, 2004), could also drive a periodic mean
774 up-canyon flow. The associated near-bottom (< 50 m) down-canyon flow could
775 also be linked to turbidity currents and river-flood-induced underflows, that

776 occur as shelf sediment descends through canyons to the ocean interior (Xu
777 & Noble, 2009; Chauvet et al., 2018). At Barkley Canyon, where large-scale
778 regional mean currents move consistently along-slope across the mouth and
779 rim of the canyon, this seems a likely explanation; however, tidal rectification
780 and turbidity currents cannot be ruled out.

781 To associate the observed mean flow characteristics with these potential forcing
782 mechanisms, correlations were computed for the observed along-canyon peri-
783 odicity and mean currents at Slope, fortnightly spring-neap tidal influence, and
784 depth-mean semidiurnal depth-band power. Correlations are inconsistent (not
785 shown), and do not suggest forcing by these sources. However, though there is
786 no obvious connection to diurnal or semidiurnal spring-neap forcing, estimates
787 of total lower-canyon transport (below -700 m) from depth- and time-mean an-
788 nual velocities result in near-zero net up-canyon flow (annually between 0.004
789 - 0.005 m/s), potentially consistent with tidal rectification theory.

790 Though along-canyon mean flow systems have been noted at other canyons, the
791 periodicity and attributed forcing comparisons at Barkley Canyon do not align
792 with other studies. It seems most likely that this circulation is driven by the
793 strong regional mean currents that exist at Slope, though tidal rectification
794 and turbidity currents may contribute. It is possible that such circulation
795 may be common in shelf-incising canyons, but that forcing is dependent on
796 unique site characteristics and regional physical processes, and so is difficult
797 to determine. Further evaluation is necessary, and beyond the scope of this
798 study.

799 6.2 Tidal forcing

800 The diurnal and semidiurnal tidal constituents are two of the greatest sources
801 of IW energy, and affect mean currents, mixing, IT and baroclinic shelf wave
802 propagation, and VICS circulation and productivity (Crawford & Thomson,
803 1984; Cummins & Oey, 1997).

804 For the diurnal constituent, there is elevated energy in the late-spring and sum-
805 mer. Results are consistent with previous studies in the region; Drakopolous
806 and Marsden (1993) associated strengthened diurnal tidal flow over the VICS
807 with increased stratification in summer, while Cummins et al. (2000) sug-
808 gest diurnal currents are seasonally responsive to the large-scale spring shift
809 to equatorward, upwelling-favourable, mean currents. Xu and Noble (2009)
810 found inter-annually consistent K_1 currents in Monterey Canyon that peaked
811 relative to the annual cycle of spring-neap tidal forcing, as observed.

812 As the diurnal (and sub-diurnal) frequency is sub-inertial, diurnal IT are

813 evanescent (trapped) to topography north of their turning latitude ($\sim 30^\circ\text{N}$),
814 unable to radiate offshore. This is consistent with the likely barotropic forcing
815 observed; Cummins and Oey (1997) found that trapped diurnal IT genera-
816 tion was prevalent on the VICS adjacent continental slope, similar to other
817 Pacific slopes (Rudnick et al., 2015) and seamounts (Robertson et al., 2017).
818 It is unlikely for there to be incident baroclinic diurnal IW or IT unless they
819 propagate along the shelf. However, if a diurnal spring-neap phase-lag of up
820 to a day is present, as potentially observed at Slope, this suggests a baro-
821 clinic generation site within about 200 km, based on a K_1 mode-1 wave speed
822 of about $c_1 \sim 2.0 \text{ m/s}$ (Crawford & Thomson, 1984). One candidate would
823 be diurnal shelf waves generated by oscillatory tidal currents near the mouth
824 of the Juan de Fuca Strait ($\sim 100 \text{ km}$ east) that propagate poleward along
825 the VICS (Crawford & Thomson, 1984; Flather, 1988). Confirmation of such
826 waves would require additional instruments along the shelf, and is beyond the
827 scope of this study. Other regions thought to be productive for baroclinic
828 diurnal waves are either disconnected from the shelf (e.g. the abyssal Juan de
829 Fuca Ridge) and cannot propagate sub-inertially to Barkley Canyon (Lavelle
830 & Cannon, 2001), or too distant for the observed phase-lag (e.g. Mendocino
831 Escarpment, 900 km south; Morozov, 2018). As there is enough uncertainty
832 in the correlations that the phase-lag could effectively be null, and considering
833 the vertically linear structure present, it is likely that the diurnal band is pri-
834 marily forced by the local barotropic spring-neap cycle, with possible seasonal
835 contributions from shelf-waves, mean current interactions, or stratification.

836 In contrast, the semidiurnal constituent is locally super-inertial, able to freely
837 propagate away from topography as IT. There could be incident remote semidiur-
838 nal IT at Barkley Canyon, contributing to the highly variable response. For
839 a semidiurnal phase-lag up to four days, as potentially observed at Slope, a
840 regional mode-1 M_2 phase speed of $c_1 \sim 3.0 \text{ m/s}$ (Zhao et al., 2016) sug-
841 gests a baroclinic generation site up to 1000 km away. A likely candidate is
842 the Mendocino Escarpment running E-W off of Northern California, one of
843 the strongest generation sites for low-mode semidiurnal IT in the northeast
844 Pacific (Althaus et al., 2003; Arbic et al., 2012; Zhao et al., 2017; Morozov,
845 2018). Strong tide-topography generated northward propagating mode-1 M_2
846 IT, along with the escarpment's location about 800 km due south of Barkley
847 Canyon (~ 3.5 days), agree reasonably with the observed phase lag. Other
848 potential semidiurnal IT generation sites are closer (e.g. the mouth of Juan
849 de Fuca Strait $\sim 100 \text{ km}$, or the abyssal Juan de Fuca Ridge $\sim 400 \text{ km}$), or are
850 somewhat obstructed by land (e.g. the Haida Gwaii Islands to the north), but
851 could contribute.

852 Furthermore, for free IW and IT, such as incident semidiurnal IT, the critical-
853 ity of the impacted topography can lead to focusing and breaking, or reflection.
854 Barkley Canyon is generally supercritical or near-critical to incident semidiurnal
855 IT (Figure 4). Critical slope regions were determined from the gradient of
856 bathymetry data obtained from the National Oceanic and Atmospheric Ad-
857 ministration (NOAA) National Centre for Environmental Information, as 3
858 arc-second resolution mean sea level depth. At the Slope mooring, the lo-
859 cal slope is $\beta \approx 0.060$, supercritical to the semidiurnal propagation angle
860 $\alpha_{M2} \approx 0.026$ at that depth (Figure 5). This suggests downward reflection
861 (CW) and focusing of incident semidiurnal IT. The Slope mooring sits adja-
862 cent to a large near-critical region below the shelf-break (Figure 4), which,
863 along with the VICS itself, is another source of observed downward semidiur-
864 nal energy (Drakopoulos & Marsden, 1993). At other slope sites, there is
865 evidence of elevated near-bottom energy-flux associated with both semidiurnal
866 IT generation and incident reflection, with similar vertical scales within a few
867 hundred metres AB (Terker et al., 2014; Xie & Chen, 2021). For the Axis
868 mooring on the canyon floor, local criticality is $\beta \approx 0.019 < \alpha_{M2} \approx 0.036$
869 (Figure 5). As such, this portion of the canyon floor is subcritical to semidiur-
870 nal IT, suggesting upward reflection (CCW). However, as the canyon walls
871 are generally supercritical, and the surrounding floor is near-critical (Figure
872 4), the propagation of semidiurnal IT at Axis is likely complex. Xu and No-
873 ble (2009) found that deep in Monterey Canyon semidiurnal IT were not only
874 scattered up-canyon along the subcritical floor, but also reflected down by the
875 supercritical walls, highly focusing semidiurnal energy near the bottom. The
876 potential for scattering, reflection, focusing, and generation of semidiurnal IT
877 all near the Axis mooring could lead to the highly 'channeled' deep-canyon
878 semidiurnal response.

879 Together, the irregular nature of the semidiurnal spring-neap phase-lag and the
880 potential for critical IT-topography interactions suggests that forcing is a mix
881 of local barotropic and incident IT. As the barotropic tide passes over Barkley
882 Canyon, near-critical slope topography generates and focuses semidiurnal IT,
883 which radiate downward from the shelf-break to the slope and canyon, where
884 further downward reflection and focusing occurs. Remote incident IT are also
885 subject to these effects, and alter observed spring-neap phase based on their
886 origin, likely Mendocino Escarpment to the south. Finally, as the little annual
887 seasonality in the local barotropic spring-neap forcing cannot explain large-
888 scale inter-annual features in the observations, such as the subtle yet consistent
889 spring increase in semidiurnal energy at Slope, secondary contributors may
890 include seasonal changes to stratification (Drakopoulos & Marsden, 1993) and
891 mean currents (Cummins et al., 2000).

892 6.3 Near-inertial forcing

893 NI IW generated by wind events are thought to be significant contributors to
894 mixing in the deep ocean, of similar magnitude to the conversion of barotropic
895 tide to baroclinic internal tide energy (Alford et al., 2012). As such effective
896 contributors to deep ocean energy, it is interesting that NI band-power can
897 be so strongly attenuated with depth at Slope, while still eliciting a deep
898 response at Axis. The timing of these events is linked, so the difference in
899 topography likely modulates the response. Thomson et al. (1990) found that
900 NI IW become increasingly attenuated as they approach slopes, absorbed by
901 strong vertical shear in the background flow associated with topographically
902 trapped oscillations. Yet observed NI IW energy is enhanced near the canyon
903 floor, not attenuated. Alford et al. (2016) note that canyon walls confine the
904 typically circular motion of NI waves, forcing them rectilinearly along-canyon.

905 It may be that canyon topography uniquely effects the modal structure of ML
906 generated NI waves. Mode-1 amplitudes up to 0.6 m/s occur after notable
907 wind events, similar to findings by Jarosz et al. (2007) in DeSoto Canyon,
908 who found that while low modes generally dominate, more NI activity is ob-
909 served when the ML is thin and high modes are prevalent. Alford et al. (2016)
910 note that high mode waves propagate downward and equatorward, while low
911 mode waves contribute more to lateral propagation of NI energy. Ultimately,
912 the downward propagation of NI IW is difficult to characterise, as there are
913 so many factors to consider, including topography, seasonal thermocline thick-
914 ness, β -plane effects, and near-surface mesoscale vorticity adjusting local f_0
915 (Alford et al., 2016). Potential secondary forcing could be mean currents or
916 lee waves of NI frequency across the mouth or rim of the canyon, where topo-
917 graphic attenuation of downward NI energy may be reduced due to the relative
918 openness of those areas, driving deep along-canyon NI currents.

919 Regarding the delayed NI deep response to wind events, D'Asaro (1995) made
920 a similar observation of an 8-10 day event, and theorised that divergence-
921 forced NI pumping at the ML base causes oscillating pressure gradients in the
922 thermocline, accelerating NI currents at depth. The rate of vertical energy
923 transfer depends on the horizontal scale of the ML NI currents, with smaller
924 horizontal scale ML currents propagating vertical energy faster. As vertical
925 modes have progressively slower horizontal group velocities, the low modes
926 propagate their energy away, first. As the low mode energy propagates away,
927 the available energy and horizontal scale of the ML inertial currents decreases.
928 Vertical energy propagation into the thermocline increases accordingly, with
929 a notable maximum associated with a timescale of the departure of modes 1
930 and 2 (up to 10-20 days), described as 'inertial beating', after which the deep

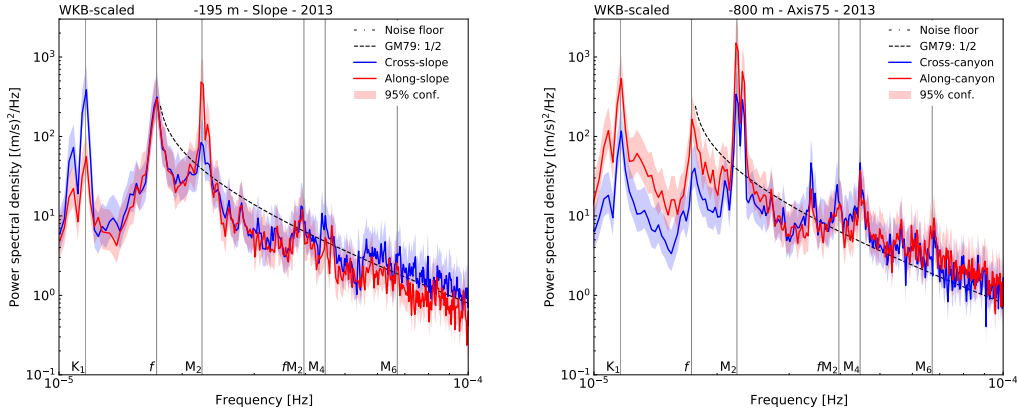


Figure 31. High frequency-resolution mid-depth PSD of WKB-scaled horizontal velocity data, for Slope (left) and Axis (right), in 2013. Frequency scale is zoomed to the tidal range. There are no additional peaks or apparent blue-shift for the NI constituent, suggesting local forcing.

931 response rapidly increases and NI energy is evenly distributed between the
 932 upper thermocline and lower depths (Gill, 1984; D'Asaro, 1995; Zervakis &
 933 Levine, 1995). The beta effect can also decrease the north-south horizontal
 934 wavenumber, l , over time, further decreasing the horizontal scale of the ML
 935 NI currents and increasing downward NI energy transfer. The radiation of NI
 936 energy to deep water is also occasionally associated with 'inertial jets' of CW
 937 relative vorticity originating near the upper pycnocline, possibly induced by
 938 mesoscale fronts (Kunze, 1985; D'Asaro, 1995; Zhai et al., 2005; Alford et al.,
 939 2016).

940 The results suggest that NI forcing is complex, dependent on variable charac-
 941 teristics of both wind events and ML processes, leading to highly intermittent
 942 seasonality, below. Small (~ 100 km) southward cold fronts and lows with con-
 943 siderable CW NI rotation are the most significant sources of ML NI flux, even
 944 more-so than synoptic-scale systems, and occur most often, yet intermittently,
 945 in fall and early-winter (D'Asaro, 1985; Alford, 2001; Voelker et al., 2020).
 946 Remote forcing is also possible, as free NI IW generated at the base of the
 947 surface mixed-layer must propagate equatorward due to the effects of turning
 948 latitudes (Alford et al., 2016). There is often a blue-shift of the f spectral
 949 peak associated with remote NI forcing (Garratt, 1977; Voelker et al., 2020);
 950 however, high frequency-resolution spectra (Figure 31) do not resolve any ad-
 951 dditional NI peaks. Wind forcing correlations may be further complicated by
 952 the location of the wind data buoy, 50 km north of Barkley Canyon. Regard-
 953 less, strong qualitative and moderate quantitative correlations suggest that

the NI observations are most responsive to wind events when the ML is thin and high-mode contributions are prevalent, particularly in the late-summer and fall. Jarosz et al. (2007) noted that seasonally variable pycnocline and ML depths can modulate NI energy by up $12\times$ when the ML is thin, affecting the stratification-dependent modes strummed by the wind induced ML NI currents. All in all, accurate quantification of NI energy is difficult. To summarise the efficacy of attempting to characterise vertical NI processes, Alford et al. (2016), when discussing the foundational Ocean Storms Experiment (D'Asaro, 1995), stated that “neither the decay of mixed-layer motions nor the rate of energy transfer into the deep ocean can adequately be predicted for the best-documented storm response on record”; needless to say, additional research is necessary.

6.4 Continuum-dissipation estimates

Topographic focusing of low-frequency IW and IT enhances energy, elevating the continuum amplitude and driving mixing (Polzin, 2004). This is indicated by the heightened amplitudes and steep spectral slopes of the observed continuum, as compared to open-ocean GM values (Figure 25). As IW energy cascades from low- (tidal and sub-inertial) to high-frequency processes, continuum energy seasonality should reflect this transfer (Polzin, 2004). At both sites, continuum energy seasonality correlations and power law fits indicate the semidiurnal constituent is the greatest contributor to dissipation; secondary contributors are the sub-diurnal band at Slope, and NI band at Axis. There are likely lesser contributions from other constituents. For continental slopes, mean currents and semidiurnal IT have both been noted to contribute to increased near-bottom dissipation rates (Nash et al., 2007; Kunze et al., 2012), as observed. Similarly, in submarine canyons, the semidiurnal constituent has been found to be the primary contributor to seasonal, near-bottom mixing (Kunze et al., 2002; Waterhouse et al., 2017); however, there is a lack of evidence for the observed deep-canyon NI IW energy, as discussed in Section 6.3. Also evident is the non-isotropic nature of the continuum, in contrast to a theoretical GM open-ocean IW field, though this departure from theory is not surprising considering the strong topographic guiding of flow.

As it is difficult to quantify turbulence, it is hoped that a connection to semidiurnal (and secondary constituent) energy may be useful for models that may not have access to data that can resolve such high-frequency processes, in slope and canyon regions. The multi-variate power law fits were found to be $\epsilon \sim M_2^{0.83 \pm 0.17} + \text{Sub}_{K1}^{0.59 \pm 0.13}$ and $\epsilon \sim M_2^{1.47 \pm 0.48} + \text{NI}^{0.24 \pm 0.06}$, for Slope and Axis, respectively. This builds on similar results by Klymak et al. (2006) at the Hawaiian Ridge, who found that near the ridge dissipation scaled with

993 semidiurnal energy as $\epsilon \sim M_2^{1.0 \pm 0.5}$. However, it is not enough to link dissipation
994 to IW and IT driven continuum energy, alone, as there are many spatially
995 and temporally variable regional processes that may also contribute, such as
996 large-scale ocean circulation, biogeochemical cycles, weather, and long-term
997 climate (Kunze, 2017). Furthermore, turbulence may be forced intermittently
998 by these phenomena (Klymak et al., 2006), making it difficult to attribute in-
999 dividual contributors over long periods. Use of the observed fits for modelling
1000 should be considered with these issues in mind, and improvements could be
1001 the subject of further research.

1002 6.5 Spectral shoulder energy

1003 The near- N spectral shoulder is a well known, yet often unresolved feature
1004 in ADCP velocity spectra. As early as 1975, Pinkel described a prominent
1005 near- N peak that widened with depth, ascribed to IW-buoyancy ringing, yet
1006 beyond the next decade (Kase & Clarke, 1978; Levine et al., 1983) subsequent
1007 observations are brief, and temporally sparse (D'Asaro et al., 2007; Pinkel,
1008 2014; Alford et al., 2016). The long-term, high-frequency sampling in this
1009 study allows for a high Nyquist frequency and low noise floor that fully expose
1010 the shoulder, continuing the discussion. Observations indicate that shoulder
1011 energy is intermittently depth dependent at Slope, and more uniformly so at
1012 Axis, similar to Pinkel's (1975) findings. There is subtle shoulder energy sea-
1013 sonality at both sites, being generally stronger in the fall, with correlations
1014 and power law fits suggesting that shoulder energy is tied to the continuum,
1015 and therefore dissipation. This agrees with previous theories, arguing that the
1016 near- N shoulder is a result of an enhanced cascade of energy from low- to high-
1017 frequency turbulent processes due to resonant wave-wave interaction, where
1018 energy collects at and above the "resonant buoyancy frequency" - approxi-
1019 mately the depth-mean value of N below the buoyancy variable thermocline
1020 (Leder, 2002). In this study, $N_0 = 4.03 \times 10^{-4}$ Hz (averaged around -900 m
1021 and varying insubstantially when expanded to the lower thermocline), central
1022 to the observed shoulder, and similar to the ~ 2 cph value of N_0 that defined
1023 the spectral shoulder (2 - 5 cph) of Kase and Clarke (1978), who modelled the
1024 near- N response with data from the GATE experiment.

1025 However, seasonal forcing of the near- N spectral shoulder is inconsistent be-
1026 tween studies. At Barkley Canyon, correlations and power law fits suggest
1027 that continuum energy is strongly linked to spectral shoulder energy. As these
1028 power law fits overlap within uncertainty for both sites (averaging $P_{Sh} \sim$
1029 $\epsilon^{0.34 \pm 0.08}$), it is possible that this relationship is independent of site topog-
1030 raphy, possibly due to the relatively small spatial scale of near- N motions.
1031 Furthermore, as continuum energy is strongly suspected to cascade from the

1032 semidiurnal constituent (and partially from secondary contributors), the same
1033 forcing should apply to the spectral shoulder as the cascade continues. Leder
1034 (2002) suggested that solitons forming in the troughs of semidiurnal IT could
1035 contribute to near- N energy, but that it is unlikely, and evidence against
1036 this theory was provided by D'Asaro et al. (2007) who found no association
1037 between shoulder energy and observed solibores. Furthermore, there are no
1038 obvious solibores noted in the Barkley Canyon observations. Pinkel (2014)
1039 suggested that sub-mesoscale currents could contribute to near- N energy, and
1040 both Leder (2002) and Alford et al. (2016) attributed enhanced high-frequency
1041 shear to wind-forced NI IW. Forcing by these constituents agrees roughly with
1042 the possible secondary contributors to observed continuum energy (sub-diurnal
1043 at Slope, and NI at Axis), but is suspiciously lacking semidiurnal influence. It
1044 is possible that the near- N spectral shoulder does receive energy from the con-
1045 tinuum, but that turbulent processes are so variable, regionally, that forcing
1046 is unique to each study site. Properly quantifying the nature of this enhanced
1047 cascade of energy is important for better understanding the effects of turbu-
1048 lence and mixing, but is beyond the scope of this study.

1049 7 Summary and conclusions

1050 It was found that there is significant influence from topography on the lo-
1051 cal IW field at both sites. Continental slope and canyon topography guides
1052 flow, with inter-annually consistent, periodic (about a week) up-canyon mean
1053 currents (-700 to -900 m) above a near-bottom down-canyon layer. There is
1054 frequency-dependent focusing of IW energy, generally up to a factor of 10, 130
1055 m AB at Slope, and up to a factor of 100, 230 m AB at Axis. The near-
1056 topography enhancement layer has unique seasonality for individual frequency
1057 constituents, and varies little inter-annually. Sub-diurnal and diurnal flows are
1058 sub-inertially trapped along topography, and the diurnal band appears to be
1059 forced locally (barotropically). The NI band is attenuated near the slope, yet
1060 elevated near the canyon bottom, with intermittent forcing that appears linked
1061 to regional wind events, high-mode propagation, and the seasonal ML depth.
1062 Free semidiurnal IT are focused and reflected near critical topography, and
1063 appear to experience both local and remote (baroclinic) forcing. The IW con-
1064 tinuum is elevated compared to the open-ocean GM spectrum (up to $7 \times$ GM),
1065 with enhanced dissipation (exceeding 10^{-8} W/kg) and diffusivity (exceeding
1066 10^{-4} m²/s) near topography. Dissipation–band-power seasonality correlations
1067 suggest a cascade of energy from the semidiurnal constituent, yielding inter-
1068 annual power law fits of $\epsilon \sim M_2^{0.42 \pm 0.29}$ at Slope, and $\epsilon \sim M_2^{0.64 \pm 0.30}$ at Axis.
1069 Improved fits accounting for secondary constituents (Sub_{K1} at Slope, and NI

at Axis) yield power law relationships of $\epsilon \sim M_2^{0.83 \pm 0.17} + \text{Sub}_{K1}^{0.59 \pm 0.13}$ at Slope, and $\epsilon \sim M_2^{1.47 \pm 0.48} + \text{NI}^{0.24 \pm 0.06}$ at Axis. There is evidence of a near- N spectral shoulder which may obtain energy from the continuum, possibly an additional step in the cascade of energy from low- to high-frequency dissipative processes. The shoulder-dissipation energy seasonality correlations yield an average, site-independent power law fit of $P_{Sh} \sim \epsilon^{0.34 \pm 0.08}$.

Unfortunately, the WKB-stretch scaling applied throughout much of the analysis is based on deep CTD casts that were made nearby (20 km S), but away from topography; the stratification profile captures the surface ML and pycnocline, but does not account for stratification adjustment near the slope or in the canyon (Figure 8). Hotchkiss and Wunsch (1982) noted increased stratification near areas of high 'topographic relief', such as the shelf-break and slopes. These highly stratified turbulent layers may more strongly experience the effects of reflection, scattering, and IT and lee-wave generation, as well as amplification of IW and IT. To properly account for the effects of depth-dependent stratification variability, further research would benefit from site specific climatology data.

Results could be further improved through increased sampling consistency between instruments (there were maintenance periods and instrument redeployments during analysis years), additional instrument sites (along the length of the canyon floor and rim), and additional overlapping comparison years between sites. Broader temporal coverage could provide insight into decadal seasonality, while additional spatial coverage would allow for observations of IW propagation. For NI wind forcing, reanalysis wind data may have provided better (fewer gaps) temporal coverage for comparison. Further research is required to: identify forcing for the periodicity of the shoaling up-canyon mean currents at Axis and the sub-diurnal range's intermittent seasonality; accurately identify sites of origin for incident baroclinic shelf-waves and IT affecting the diurnal and semidiurnal responses; better quantify the downward propagation of NI IW energy from the ML to the interior; and, improve power law fits of dissipation and near- N spectral shoulder energy to better model the cascade of energy from low- to high-frequency turbulent mixing.

Barkley Canyon is a dynamic continental slope and submarine canyon region with physical processes that are heavily influenced by topography. Slopes and canyons are known as hot-spots for IT generation and IW-driven turbulence, contributing significantly to regional transport of energy, shelf productivity, and even large-scale ocean circulation and climate effects. As regional currents, tides, and wind all contribute to an energetic local IW field, the Barkley Canyon portion of ONC's NEPTUNE cabled observatory is an important data

1109 network for understanding the effects of topography-IW interactions on the
1110 VICS. Furthermore, results here may be valuable for characterising mixing
1111 processes at other slope and canyon sites, and for better estimating the global
1112 IW and IT energy budget. It is hoped that this study has provided valuable
1113 insight leading to further research and collaboration, and improved knowledge
1114 of the importance of shelf-incising canyon regions as fundamental to both re-
1115 gional and large-scale physical ocean processes.

¹¹¹⁶ **8 Appendix A: Supplemental plots**

¹¹¹⁷ **8.1 Wind comparisons**

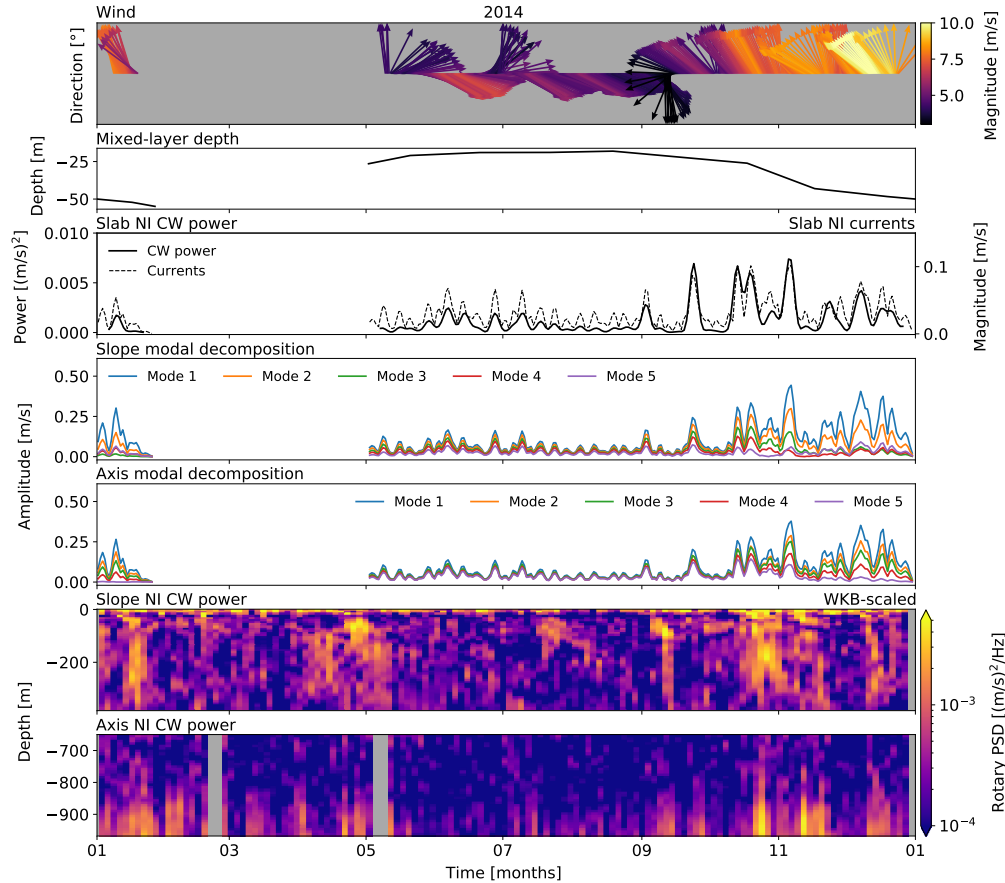


Figure 32. NI forcing analysis for 2014. Panels are (i) wind direction and amplitude, (ii) monthly-averaged ML depth for Line P station 3 as determined by Li et al. (2005), (iii) slab model NI CW power and NI currents, (iv, v) seasonal mode amplitudes for Slope and Axis, and (vi, vii) band-integrated NI CW power at Slope and Axis. There appears to be a complex relationship between the wind, ML, slab currents, and mode amplitudes in driving the NI observations, with the most obvious effects in the fall.

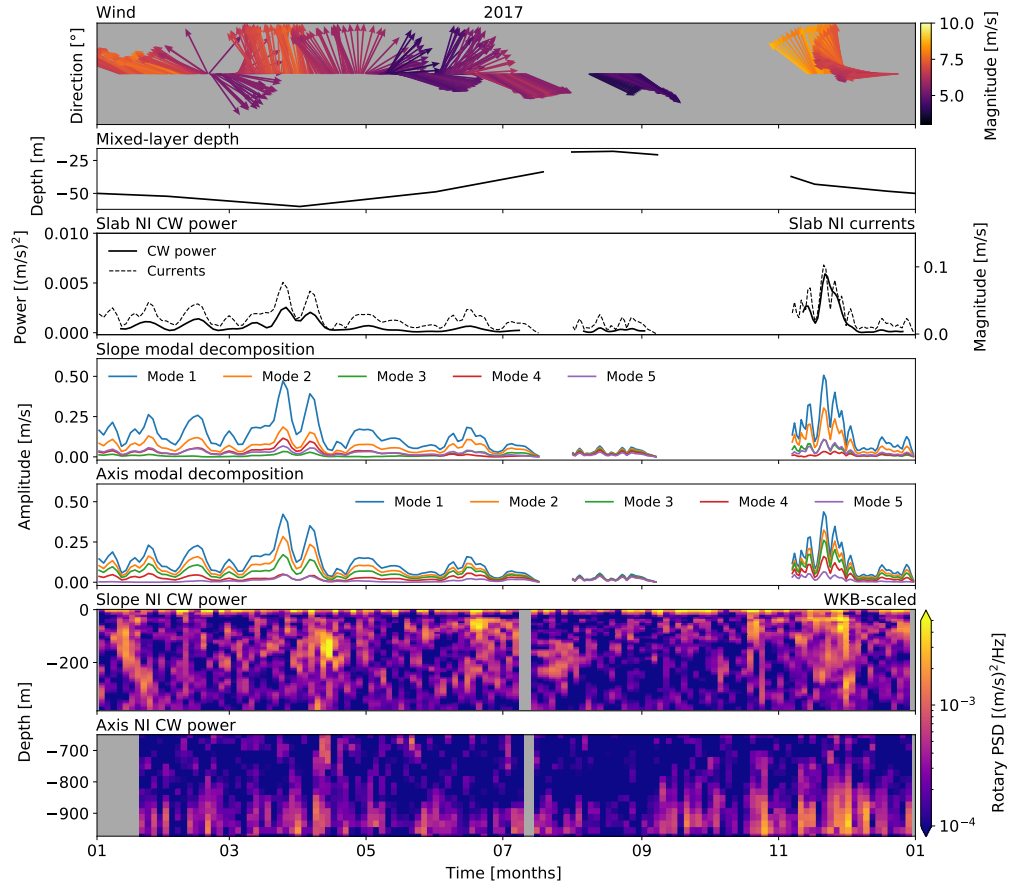


Figure 33. NI forcing analysis for 2017. Panels are (i) wind direction and amplitude, (ii) monthly-averaged ML depth for Line P station 3 as determined by Li et al. (2005), (iii) slab model NI CW power and NI currents, (iv, v) seasonal mode amplitudes for Slope and Axis, and (vi, vii) band-integrated NI CW power at Slope and Axis. There appears to be a complex relationship between the wind, ML, slab currents, and mode amplitudes in driving the NI observations, with the most obvious effects in the fall.

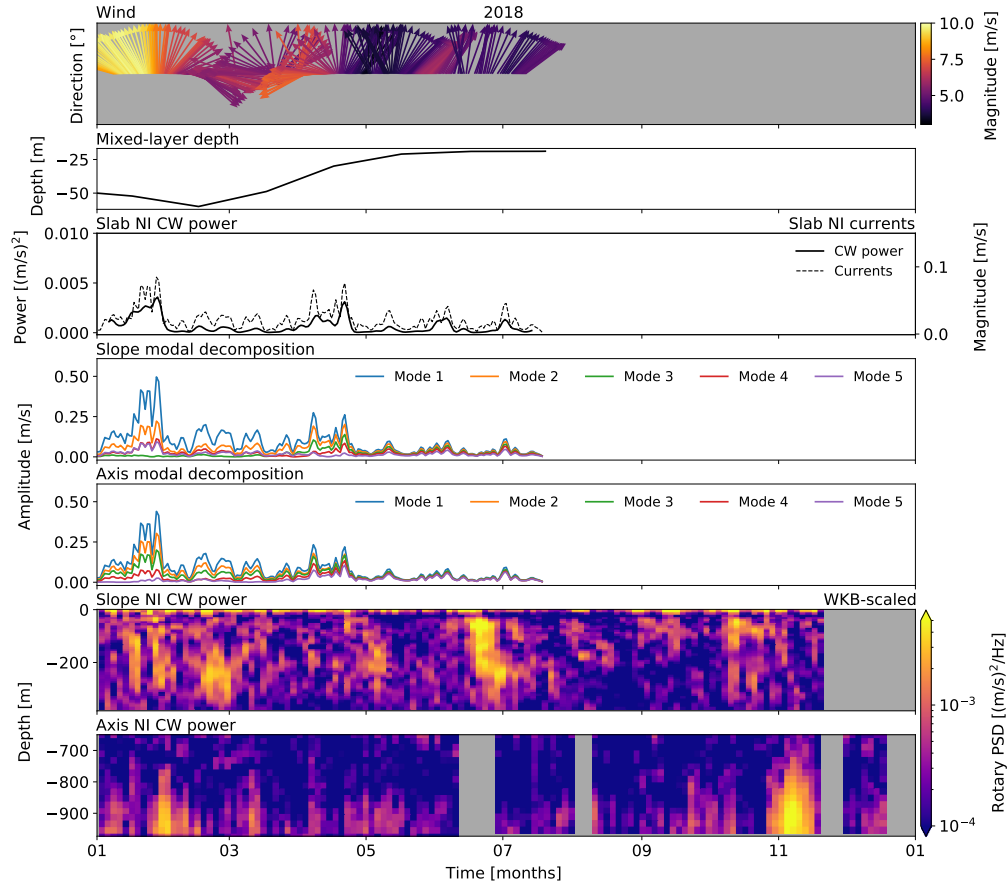


Figure 34. NI forcing analysis for 2018. Panels are (i) wind direction and amplitude, (ii) monthly-averaged ML depth for Line P station 3 as determined by Li et al. (2005), (iii) slab model NI CW power and NI currents, (iv, v) seasonal mode amplitudes for Slope and Axis, and (vi, vii) band-integrated NI CW power at Slope and Axis. There appears to be a complex relationship between the wind, ML, slab currents, and mode amplitudes in driving the NI observations, with the most obvious effects in the fall.

9 References

- 1118 1119 Alford, M. H. (2001). Internal swell generation: The spatial distribution of
1120 energy flux from the wind to mixed layer near-inertial motions. *Journal of*
1121 *Physical Oceanography*, 31(8 PART 2), 2359–2368. <https://doi.org/10.1175/1520-0485>
- 1122 1123 Alford, M. H., MacKinnon, J. A., Zhao, Z., Pinkel, R., Klymak, J., & Peacock, T. (2007). Internal waves across the Pacific. *Geophysical Research Letters*, 34(24), 24601. <https://doi.org/10.1029/2007GL031566>
- 1124 1125 1126 1127 1128 Alford, M. H. (2003). Improved global maps 54-year history of wind-work on ocean inertial motions. *Geophysical Research Letters*, 30(8), 1424. <https://doi.org/10.1029/2002GL016614>
- 1129 1130 1131 Alford, M. H. (2020). Revisiting near-inertial wind work: Slab models, relative stress, and mixed layer deepening. *Journal of Physical Oceanography*, 50(11), 3141–3156. <https://doi.org/10.1175/JPO-D-20-0105.1>
- 1132 1133 1134 1135 Alford, M. H., Cronin, M. F., & Klymak, J. M. (2012). Annual cycle and depth penetration of wind-generated near-inertial internal waves at ocean station papa in the northeast pacific. *Journal of Physical Oceanography*, 42(6), 889–909. <https://doi.org/10.1175/JPO-D-11-092.1>
- 1136 1137 1138 1139 Alford, M. H., Mackinnon, J. A., Simmons, H. L., & Nash, J. D. (2016). Near-Inertial Internal Gravity Waves in the Ocean. *Annual Review of Marine Science*, 8, 95–123. <https://doi.org/10.1146/annurev-marine-010814-015746>
- 1140 1141 1142 1143 Alford, M. h., Shcherbina, A. Y., & Gregg, M. C. (2013). Observations of Near-Inertial Internal Gravity Waves Radiating from a Frontal Jet. *Journal of Physical Oceanography*, 43(6), 1209–1224. <https://doi.org/10.1175/JPO-D-12-0146.1>
- 1144 1145 1146 Alford, M. H., & Zhao, Z. (2007). Global patterns of low-mode internal-wave propagation. Part I: Energy and energy flux. *Journal of Physical Oceanography*, 37(7), 1829–1848. <https://doi.org/10.1175/JPO3085.1>
- 1147 1148 1149 1150 Allen, S. E., Vindeirinho, C., Thomson, R. E., Foreman, M. G. G., & Mackas, D. L. (2001). Physical and biological processes over a submarine canyon during an upwelling event. *Canadian Journal of Fisheries and Aquatic Sciences*, 58(4), 671–684. <https://doi.org/10.1139/f01-008>
- 1151 1152 Althaus, A. M., Kunze, E., & Sanford, T. B. (2003). Internal tide radiation from Mendocino escarpment. *Journal of Physical Oceanography*, 33(7),

- 1153 1510–1527. <https://doi.org/10.1175/1520-0485>
- 1154 Anstey, K. (2022). Internal waves at Barkley Canyon. Retrieved from GitHub
1155 website: https://github.com/kurtisanstey/internal_waves_barkley_canyon
- 1156 Arbic, B. K., Richman, J. G., Shriver, J. F., Timko, P. G., Joseph Metzger, E.,
1157 & Wallcraft, A. J. (2012). Global modeling of internal tides within an
1158 eddying ocean general circulation model. *Oceanography*, 25(2), 20–29.
1159 <https://doi.org/10.5670/oceanog.2012.38>
- 1160 Brink, K. H. (1991). Coastal-trapped waves and wind-driven currents over the
1161 continental shelf. *Annual Review of Fluid Mechanics*, 23(1), 389–412.
1162 <https://doi.org/10.1146/annurev.fl.23.010191.002133>
- 1163 Burrier, D. A. (2019). The Internal Wave Dynamics of Barkley Submarine
1164 Canyon. San Jose State University.
- 1165 Cabrera, F., Ogata, B., Sastri, A. R., Heesemann, M., Mihály, S., Galbraith,
1166 M., & Morley, M. G. (2018). High-frequency observations from a deep-
1167 sea cabled observatory reveal seasonal overwintering of *Neocalanus* spp.
1168 in Barkley Canyon, NE Pacific: Insights into particulate organic carbon
1169 flux. *Progress in Oceanography*, 169, 120–137. <https://doi.org/10.1016/j.pocean.2018.06.001>
- 1171 Carter, G. S., & Gregg, M. C. (2002). Intense, variable mixing near the head
1172 of Monterey Submarine Canyon. In *Journal of Physical Oceanography*
1173 (Vol. 32). <https://doi.org/10.1175/1520-0485>
- 1174 Chauvet, P., Metaxas, A., Hay, A. E., & Matabos, M. (2018). Annual and
1175 seasonal dynamics of deep-sea megafaunal epibenthic communities in
1176 Barkley Canyon (British Columbia, Canada): A response to climatology,
1177 surface productivity and benthic boundary layer variation. *Progress in
1178 Oceanography*, 169, 89–105. <https://doi.org/10.1016/j.pocean.2018.04.002>
- 1179 Crawford, W. R., & Thomson, R. E. (1984). Diurnal-Period Continental Shelf
1180 Waves along Vancouver Island: A Comparison of Observations with The-
1181 oretical Models. *Journal of Physical Oceanography*, 14(10), 1629–1646.
1182 <https://doi.org/10.1175/1520-0485>
- 1183 Cummins, P. F., Masson, D., & Foreman, M. G. G. (2000). Stratification and
1184 mean flow effects on diurnal tidal currents off Vancouver Island. *Journal
1185 of Physical Oceanography*, 30(1), 15–30. <https://doi.org/10.1175/1520-0485>
- 1187 Cummins, P. F., & Oey, L. Y. (1997). Simulation of barotropic and baroclinic

- 1188 tides off northern British Columbia. *Journal of Physical Oceanography*,
1189 27(5), 762–781. <https://doi.org/10.1175/1520-0485>
- 1190 D'Asaro, E. A. (1985). The energy flux from the wind to near-inertial motions
1191 in the surface mixed layer. *J. Phys. Oceanogr.*, 15(8, Aug. 1985),
1192 1043–1059. <https://doi.org/10.1175/1520-0485>
- 1193 D'Asaro, E. A. (1995). Upper-ocean inertial currents forced by a strong storm.
1194 Part III: interaction of inertial currents and mesoscale eddies. *Journal of
1195 Physical Oceanography*, 25(11 Part II), 2953–2958. <https://doi.org/10.1175/1520-0485>
- 1197 D'Asaro, E. A., Lien, R. C., & Henyey, F. (2007). High-frequency internal
1198 waves on the Oregon continental shelf. *Journal of Physical Oceanography*,
1199 37(7), 1956–1967. <https://doi.org/10.1175/JPO3096.1>
- 1200 Doya, C., Aguzzi, J., Pardo, M., Matabos, M., Company, J. B., Costa, C., ...
1201 Canals, M. (2014). Diel behavioral rhythms in sablefish (*Anoplopoma
1202 fimbria*) and other benthic species, as recorded by the Deep-sea cabled
1203 observatories in Barkley canyon (NEPTUNE-Canada). *Journal of Marine
1204 Systems*, 130, 69–78. <https://doi.org/10.1016/j.jmarsys.2013.04.003>
- 1205 Drakopoulos, P. G., & Marsden, R. F. (1993). The internal tide off the west
1206 coast of Vancouver Island. *Journal of Physical Oceanography*, 23(4),
1207 758–775. <https://doi.org/10.1175/1520-0485>
- 1208 Flather, R. A. (1988). A numerical model investigation of tides and diurnal-
1209 period continental shelf waves along Vancouver Island. *J. Phys. Oceanogr.*,
1210 18(1, Jan. 1988), 115–139. <https://doi.org/10.1175/1520-0485>
- 1211 Garrett, C., & Kunze, E. (2007). Internal tide generation in the deep ocean.
1212 Annual Review of Fluid Mechanics, 39, 57–87. <https://doi.org/10.1146/annurev.fluid.39.050905.110227>
- 1214 Garrett, C. (2005). 2004 Program of Study: Tides Course Lectures Fellows
1215 Project Reports.
- 1216 Gemmrich, J., & Klymak, J. M. (2015). Dissipation of internal wave energy
1217 generated on a critical slope. *Journal of Physical Oceanography*, 45(9),
1218 2221–2238. <https://doi.org/10.1175/JPO-D-14-0236.1>
- 1219 Gill, A. E. (1984). On the Behavior of Internal Waves in the Wakes of Storms.
1220 *Journal of Physical Oceanography*, 14(7), 1129–1151. <https://doi.org/10.1175/1520-0485>
- 1221

- 1222 Gonella, J. (1972). A rotary-component method for analysing meteorological
1223 and oceanographic vector time series. In Deep-Sea Research and
1224 Oceanographic Abstracts (Vol. 19). <https://doi.org/10.1016/0011-7471>
- 1225 Gregg, M. C. (1989). Scaling turbulent dissipation in the thermocline. *Journal
1226 of Geophysical Research*, 94(C7), 9686. [https://doi.org/10.1029/jc094ic0
7p09686](https://doi.org/10.1029/jc094ic0
1227 7p09686)
- 1228 Hotchkiss, F. S., & Wunsch, C. (1982). Internal waves in Hudson Canyon with
1229 possible geological implications. *Deep Sea Research Part A, Oceanographic
1230 Research Papers*, 29(4), 415–442. [https://doi.org/10.1016/0198-
0149](https://doi.org/10.1016/0198-
1231 0149)
- 1232 Jarosz, E., Hallock, Z. R., & Teague, W. J. (2007). Near-inertial currents in the
1233 DeSoto Canyon region. *Continental Shelf Research*, 27(19), 2407–2426.
1234 <https://doi.org/10.1016/j.csr.2007.06.014>
- 1235 Juniper, S. K., Matabos, M., Mihály, S., Ajayamohan, R. S., Gervais, F., &
1236 Bui, A. O. V. (2013). A year in Barkley Canyon: A time-series observatory
1237 study of mid-slope benthos and habitat dynamics using the NEPTUNE Canada
1238 network. *Deep-Sea Research Part II: Topical Studies in
1239 Oceanography*, 92, 114–123. <https://doi.org/10.1016/j.dsr2.2013.03.038>
- 1240 Käse, R. H., & Allyn Clarke, R. (1978). High frequency internal waves in the
1241 upper thermocline during GATE. *Deep-Sea Research*, 25(9), 815–825.
1242 <https://doi.org/10.1016/0146-6291>
- 1243 Klymak, J. M., Alford, M. H., Pinkel, R., Lien, R. C., Yang, Y. J., & Tang,
1244 T. Y. (2011). The breaking and scattering of the internal tide on a
1245 continental slope. *Journal of Physical Oceanography*, 41(5), 926–945.
1246 <https://doi.org/10.1175/2010JPO4500.1>
- 1247 Klymak, J. M., Moum, J. N., Nash, J. D., Kunze, E., Girton, J. B., Carter,
1248 G. S., ... Gregg, M. C. (2006). An estimate of tidal energy lost to
1249 turbulence at the Hawaiian Ridge. *Journal of Physical Oceanography*,
1250 36(6), 1148–1164. <https://doi.org/10.1175/JPO2885.1>
- 1251 Kundu, P. K., & Cohen, I. (2008). Fluid mechanics. (4th ed.). Academic
1252 Press.
- 1253 Kunze, E. (1985). Near-Inertial Wave Propagation In Geostrophic Shear.
1254 *Journal of Physical Oceanography*, 15(5), 544–565. [https://doi.org/10.11
75/1520-0485](https://doi.org/10.11
1255 75/1520-0485)
- 1256 Kunze, E. (2017). Internal-wave-driven mixing: Global geography and bud-

- 1257 gets. *Journal of Physical Oceanography*, 47(6), 1325–1345. <https://doi.org/10.1175/JPO-D-16-0141.1>
- 1259 Kunze, E., Mackay, C., Mcphee-Shaw, E. E., Morrice, K., Girton, J. B., &
1260 Terker, S. R. (2012). Turbulent mixing and exchange with interior wa-
1261 ters on sloping boundaries. *Journal of Physical Oceanography*, 42(6),
1262 910–927. <https://doi.org/10.1175/JPO-D-11-075.1>
- 1263 Kunze, E., Rosenfeld, L. K., Carter, G. S., & Gregg, M. C. (2002). Internal
1264 waves in Monterey Submarine Canyon. *Journal of Physical Oceanogra-
1265 phy*, 32(6), 1890–1913. <https://doi.org/10.1175/1520-0485>
- 1266 Lamb, K. G. (2014). Internal wave breaking and dissipation mechanisms
1267 on the continental slope/shelf. *Annual Review of Fluid Mechanics*, 46,
1268 231–254. <https://doi.org/10.1146/annurev-fluid-011212-140701>
- 1269 Lavelle, J. W., & Cannon, G. A. (2001). On subinertial oscillations trapped
1270 by the Juan de Fuca Ridge, northeast Pacific. In *Journal of Geophysical
1271 Research: Oceans* (Vol. 106). <https://doi.org/10.1029/2001jc000865>
- 1272 Leder, N. (2002). Wind-induced internal wave dynamics near the Adriatic shelf
1273 break. In *Continental Shelf Research* (Vol. 22). <https://doi.org/10.1016/S0278-4343>
- 1275 Levine, M. D. (2002). A modification of the Garrett-Munk internal wave spec-
1276 trum. *Journal of Physical Oceanography*, 32(11), 3166–3181. <https://doi.org/10.1175/1520-0485>
- 1278 Li, M., Myers, P. G., & Freeland, H. (2005). An examination of historical
1279 mixed layer depths along Line P in the Gulf of Alaska. *Geophysical
1280 Research Letters*, 32(5), 1–4. <https://doi.org/10.1029/2004GL021911>
- 1281 Martini, K. I., Alford, M. H., Kunze, E., Kelly, S. M., & Nash, J. D. (2011).
1282 Observations of internal tides on the oregon continental slope. *Journal of
1283 Physical Oceanography*, 41(9), 1772–1794. <https://doi.org/10.1175/2011JPO4581.1>
- 1285 Martini, K. I., Alford, M. H., Kunze, E., Kelly, S. M., & Nash, J. D. (2013). In-
1286 ternal bores and breaking internal tides on the Oregon continental slope.
1287 *Journal of Physical Oceanography*, 43(1), 120–139. <https://doi.org/10.1175/JPO-D-12-030.1>
- 1289 Mihaly, S. F., Thomson, R. E., & Rabinovich, A. B. (1998). Evidence for non-
1290 linear interaction between internal waves of inertial and semidiurnal fre-
1291 quency. *Geophysical Research Letters*, 25(8), 1205–1208. <https://doi.org/10.1029/1998GL000001>

- 1292 /10.1029/98GL00722
- 1293 Morozov, E. G. (2018). Semidiurnal Internal Wave Global Field; Global Esti-
1294 mates of Internal Tide Energy. In *Oceanic Internal Tides: Observations,
1295 Analysis and Modeling* (pp. 263-291). [https://doi.org/10.1007/978-3-
 319-73159-9_8](https://doi.org/10.1007/978-3-
1296 319-73159-9_8)
- 1297 Munk, W., & Garrett, C. (1979). Internal Waves and Small-Scale Processes.
1298 In C. Wunsch (Ed.), *Evolution of Physical Oceanography*.
- 1299 Munk, W., & Wunsch, C. (1998). Abyssal recipes II: Energetics of tidal and
1300 wind mixing. *Deep-Sea Research Part I: Oceanographic Research Papers*,
1301 45(12), 1977–2010. <https://doi.org/10.1016/S0967-0637>
- 1302 Nash, J. D., Kunze, E., Toole, J. M., & Schmitt, R. W. (2004). Internal tide
1303 reflection and turbulent mixing on the continental slope. In *Journal of
1304 Physical Oceanography* (Vol. 34). <https://doi.org/10.1175/1520-0485>
- 1305 Petrunio, E. T., Rosenfeld, L. K., & Paduan, J. D. (1998). Observations of
1306 the internal tide in Monterey Canyon. *Journal of Physical Oceanography*,
1307 28(10), 1873–1903. <https://doi.org/10.1175/1520-0485>
- 1308 Pinkel, R. (1975). Upper ocean internal wave observations from Flip. *Journal
1309 of Geophysical Research*, 80(27), 3892–3910. <https://doi.org/10.1029/jc080i027p03892>
- 1311 Pinkel, R. (2014). Vortical and internal wave shear and strain. *Journal of
1312 Physical Oceanography*, 44(8), 2070–2092. <https://doi.org/10.1175/JPO-D-13-090.1>
- 1314 Polzin, K. L., & Lvov, Y. V. (2011). Toward regional characterizations of
1315 the oceanic internal wavefield. *Reviews of Geophysics*, 49(4), 4003.
1316 <https://doi.org/10.1029/2010RG000329>
- 1317 Polzin, K. L., Toole, J. M., Ledwell, J. R., & Schmitt, R. W. (1997). Spatial
1318 variability of turbulent mixing in the abyssal ocean. *Science*, 276(5309),
1319 93–96. <https://doi.org/10.1126/science.276.5309.93>
- 1320 Polzin, K. (2004). A heuristic description of internal wave dynamics. *Journal
1321 of Physical Oceanography*, 34(1), 214–230. [https://doi.org/10.1175/1520-0485](https://doi.org/10.1175/1520-
1322 0485)
- 1323 Robertson, R., Dong, J., & Hartlipp, P. (2017). Diurnal Critical Latitude and
1324 the Latitude Dependence of Internal Tides, Internal Waves, and Mixing
1325 Based on Barcoo Seamount. *Journal of Geophysical Research: Oceans*,
1326 122(10), 7838–7866. <https://doi.org/10.1002/2016JC012591>

- 1327 Rudnick, D. L., Gopalakrishnan, G., & Cornuelle, B. D. (2015). Cyclonic eddies in the Gulf of Mexico: Observations by underwater gliders and simulations by numerical model. *Journal of Physical Oceanography*, 45(1), 313–326. <https://doi.org/10.1175/JPO-D-14-0138.1>
- 1331 Sun, H., & Kunze, E. (1999). Internal wave-wave interactions. Part I: The role of internal wave vertical divergence. *Journal of Physical Oceanography*, 29(11), 2886–2904. <https://doi.org/10.1175/1520-0485>
- 1334 Terker, S. R., Girton, J. B., Kunze, E., Klymak, J. M., & Pinkel, R. (2014). Observations of the internal tide on the California continental margin near Monterey Bay. *Continental Shelf Research*, 82, 60–71. <https://doi.org/10.1016/j.csr.2014.01.017>
- 1338 Thomson, R. E., & Crawford, W. R. (1982). The Generation of Diurnal Period Shelf Waves by Tidal Currents in: *Journal of Physical Oceanography Volume 12 Issue 7 (1982)*. *Journal of Physical Oceanography*, 12(7). Retrieved from https://journals-ametsoc-org.ezproxy.library.uvic.ca/view/journals/phoc/12/7/1520-0485_1982_012_0635_tgodps_2_0_co_2.xml?tab_body=pdf
- 1344 Thomson, R. E., & Emery, W. J. (2014). Data Analysis Methods in Physical Oceanography: Third Edition. In *Data Analysis Methods in Physical Oceanography: Third Edition (Third)*. <https://doi.org/10.1016/C2010-0-66362-0>
- 1348 Thomson, R. E., & Fine, I. V. (2003). Estimating mixed layer depth from oceanic profile data. *Journal of Atmospheric and Oceanic Technology*, 20(2), 319–329. <https://doi.org/10.1175/1520-0426>
- 1351 Thomson, R. E., & Krassovski, M. V. (2015). Remote alongshore winds drive variability of the California Undercurrent off the British Columbia-Washington coast. *Journal of Geophysical Research: Oceans*, 120(12), 8151–8176. <https://doi.org/10.1002/2015JC011306>
- 1355 Thomson, R. E., Roth, S. E., & Dymond, J. (1990). Near-inertial motions over a mid-ocean ridge: Effects of topography and hydrothermal plumes. *Journal of Geophysical Research*, 95(C5), 7261. <https://doi.org/10.1029/jc095ic05p07261>
- 1359 Voelker, G. S., Olbers, D., Walter, M., Mertens, C., & Myers, P. G. (2020). Estimates of wind power and radiative near-inertial internal wave flux: The hybrid slab model and its application to the North Atlantic. *Ocean Dynamics*, 70(11), 1357–1376. <https://doi.org/10.1007/s10236-020-01388-y>

- 1363 Waterhouse, A. F., Mackinnon, J. A., Musgravea, R. C., Kelly, S. M., Pick-
1364 ering, A., & Nash, J. (2017). Internal tide convergence and mixing in a
1365 submarine canyon. *Journal of Physical Oceanography*, 47(2), 303–322.
1366 <https://doi.org/10.1175/JPO-D-16-0073.1>
- 1367 Xie, X., & Chen, D. (2021). Near-surface reflection and nonlinear effects
1368 of low-mode internal tides on a continental slope. *Journal of Physi-
1369 cal Oceanography*, 51(4), 1037–1051. [https://doi.org/10.1175/JPO-D-20-0197.1](https://doi.org/10.1175/JPO-D-
1370 20-0197.1)
- 1371 Xu, J. P., & Noble, M. A. (2009). Currents in monterey submarine canyon.
1372 *Journal of Geophysical Research: Oceans*, 114(3), 3004. [https://doi.org/
1373 10.1029/2008JC004992](https://doi.org/10.1029/2008JC004992)
- 1374 Zervakis, V., & Levine, M. D. (1995). Near-inertial energy propagation from
1375 the mixed layer: theoretical considerations. *Journal of Physical Oceanog-
1376 raphy*, 25(11 Part II), 2872–2889. <https://doi.org/10.1175/1520-0485>
- 1377 Zhai, X., Greatbatch, R. J., & Zhao, J. (2005). Enhanced vertical propagation
1378 of storm-induced near-inertial energy in an eddying ocean channel model.
1379 *Geophysical Research Letters*, 32(18), 1–4. [https://doi.org/10.1029/2005
1380 GL023643](https://doi.org/10.1029/2005GL023643)
- 1381 Zhao, Z., Alford, M. H., Girton, J. B., Rainville, L., & Simmons, H. L. (2016).
1382 Global observations of open-ocean mode-1 M2 internal tides. *Journal of
1383 Physical Oceanography*, 46(6), 1657–1684. [https://doi.org/10.1175/JPO-D-15-0105.1](https://doi.org/10.1175/JPO-
1384 D-15-0105.1)
- 1385 Zheng, J., Tian, J., & Liang, H. (2017). Observation of near-inertial internal
1386 waves on the continental slope in the northwestern South China Sea.
1387 *Journal of Ocean University of China*, 16(2), 184–190. [https://doi.org/10
1388 .1007/s11802-017-3153-7](https://doi.org/10.1007/s11802-017-3153-7)